nature structural & molecular biology

Article

https://doi.org/10.1038/s41594-023-01033-4

Sperm chromatin structure and reproductive fitness are altered by substitution of a single amino acid in mouse protamine 1

Received: 9 September 2021

Accepted: 12 June 2023

Published online: 17 July 2023

Check for updates

Lindsay Moritz[1,2,13], Samantha B. Schon[3,13], Mashiat Rabbani[2], Yi Sheng[4], Ritvija Agrawal[5], Juniper Glass-Klaiber[6], Caleb Sultan[2], Jeannie M. Camarillo[7], Jourdan Clements[2], Michael R. Baldwin[8], Adam G. Diehl[9], Alan P. Boyle[2,9], Patrick J. O'Brien[8], Kaushik Ragunathan[10], Yueh-Chiang Hu[11], Neil L. Kelleher[7], Jayakrishnan Nandakumar[5], Jun Z. Li[2,9], Kyle E. Orwig[4], Sy Redding[6,14] & Saher Sue Hammoud[1,2,3,12,14]

Conventional dogma presumes that protamine-mediated DNA compaction in sperm is achieved by electrostatic interactions between DNA and the arginine-rich core of protamines. Phylogenetic analysis reveals several non-arginine residues conserved within, but not across species. The significance of these residues and their post-translational modifications are poorly understood. Here, we investigated the role of K49, a rodent-specific lysine residue in protamine 1 (P1) that is acetylated early in spermiogenesis and retained in sperm. In sperm, alanine substitution (P1(K49A)) decreases sperm motility and male fertility—defects that are not rescued by arginine substitution (P1(K49R)). In zygotes, P1(K49A) leads to premature male pronuclear decompaction, altered DNA replication, and embryonic arrest. In vitro, P1(K49A) decreases protamine–DNA binding and alters DNA compaction and decompaction kinetics. Hence, a single amino acid substitution outside the P1 arginine core is sufficient to profoundly alter protein function and developmental outcomes, suggesting that protamine non-arginine residues are essential for reproductive fitness.

Spermatogenesis is a highly regulated differentiation process, in which spermatogonial stem cells give rise to mature haploid spermatozoa throughout life. In its final stage (spermiogenesis), when haploid round spermatids elongate to form sperm, the chromatin composition transitions in a stepwise fashion from a nucleosome-based to a protamine-based chromatin state. It begins with the exchange of canonical histones for testis-specific histone variants such as spermatid-specific linker histone H1-like protein (HILS1), H2AL1 and H2AL2, testis specific H2B (TH2B) and the histone H3T variant[1–7]. During this transition, histones (including canonical and testis-specific variants) acquire post-translational modifications (PTMs), notably hyperacetylation of H4[8,9] and ubiquitination of H2A/H2B[10–12], which initiates loosening of the chromatin structure to facilitate the incorporation of transition proteins 1 (TNP1) and 2 (TNP2), which are subsequently replaced by protamines[4,13,14].

Protamines are small, arginine-rich, sperm-specific structural proteins that wrap 90–95% of the mammalian sperm genome[15,16] and are essential for sperm chromatin packaging and fertility[17–21]. Most mammals, including mice and humans, express two forms of protamine: P1 is directly expressed in its mature form, whereas protamine 2 (P2) is

A full list of affiliations appears at the end of the paper. e-mail: hammou@med.umich.edu

expressed as a longer precursor (pro P2) that is initially deposited onto DNA but then selectively cleaved to produce its mature form (P2)[22,23]. Studies in both mice and humans have verified that maintaining a species-specific ratio of P1:P2 (1:1 in humans, 1:2 in mice) is necessary for fertility; conversely, decreased fertility and poor embryonic development correlate with alterations in this ratio[24–26].

At a more fundamental level, how mammalian protamines induce DNA condensation and subsequent decondensation in the zygote is less well understood. Much of our understanding of protamine–DNA dynamics arises from early in vitro studies that used either salmon or bull sperm, both of which express only one form of protamine[27–31]. However, most mammalian genomes encode multiple protamine proteins (P1, P2, and/or P3) that may engage in complex inter- and intramolecular interactions between different protamine forms, which cannot be captured or monitored in species that have a single protamine protein or species that lack cysteine residues (like salmon)[27,29,31]. Hence, our understanding of the complex, multi-protamine packaging system remains limited because it has been assumed that the biochemical and biophysical properties of all protamines are conserved owing to the high percentage of arginines, despite striking differences in amino acid sequence and composition. Therefore, it is unlikely that salmon or bull protamine biology can accurately describe functional differences in the kinetics of mammalian protamines or systems that employ a dual protamine (P1/P2) packaging system[32–34].

Given the basic nature of protamine proteins and evolutionary selection for high arginine content, studies of protamine–DNA interactions have mainly focused on arginine residues, leaving our understanding of functional roles for other residues or protamine PTMs limited[35–40]. Protamine phosphorylation during spermiogenesis was presumed to modulate protamine–DNA dynamics and maximize chromatin compaction[22,41–43]. More recently, Gou et. al. reported that phosphorylation of P1 serine residues during embryogenesis weakens protamine–DNA interactions to allow male pronuclear remodeling and protamine-to-histone exchange, in support of electrostatic interactions being primary regulators of sperm chromatin organization[44].

Here, we report the presence of acetylation on P1 Lys49—a rodent-specific residue—that is acquired in early elongating spermatids and persists in mature sperm. Mice with an alanine substitution at K49 (P1(K49A)) are subfertile, with alterations in sperm chromatin composition and defective histone eviction, leading to premature decondensation of paternal chromatin in the zygote accompanied by defects in DNA replication, increased DNA damage, and embryonic arrest at or before the morula stage. In vitro, K49A mutant protein is associated with reduced DNA binding affinity, slower DNA compaction, and accelerated DNA decompaction. Because defects in sperm quality in K49A mice were not rescued by an arginine substitution, we conclude that charge alone is not responsible for the defects, but that instead the modification itself or a structural conformation induced by lysine acetylation is required to ensure mouse sperm packaging. Taken together, our data establish that species-specific protamine–DNA interactions are not exclusively governed by electrostatics, and it is possible that protamine residues instruct species-specific genome packaging and unpackaging in the embryo.

Results

Post-translational modifications on P1 are lineage-specific

Previous studies identified P1 and P2 PTMs of unknown function in human and mouse mature sperm[38,39,41,44]. Because sperm are transcriptionally quiescent, PTMs cannot regulate transcription, and we therefore set out to investigate their alternative functions. Using mass spectrometry, we confirmed previously identified P1 modifications and identified additional modifications, such as acetylated K49 (P1(K49ac)) (Supplementary Table 1 and Fig. 1a). When we constructed a phylogenetic tree across the orders Rodentia, Primate, and Artiodactyla to gain a deeper understanding of sequence conservation of PTM-bearing sites (Fig. 1b), we found that the P1 S9 position is highly conserved, and its phosphorylation is well established in both mouse and human, indicative of a necessary function across species[38,40]. By contrast, modified S43, T45, K49, and K50, in the carboxy terminus, are highly conserved in the mouse lineage (but not in more distant species, Fig. 1b and Extended Data Fig. 1a), and of those, we set out to specifically explore the functional role of K49 in the mouse germline.

P1(K49ac) is acquired in a stage-specific manner

To investigate K49 acetylation in sperm, we generated a polyclonal anti-P1(K49ac) antibody, which detects a distinct band in immunoblots of acid-extracted protein from mature sperm. When outcompeted by an acetylated P1 K49 peptide, this band was lost, but this was not the case when a peptide from an unrelated protein, or a non-acetylated P1 peptide, was used (Extended Data Fig. 1b). Consistently, anti-K49ac failed to detect mutant P1 protein in $P1^{K49A/K49A}$ sperm lysates, confirming antibody specificity (Extended Data Fig. 1c). To determine when during spermatogenesis P1(K49ac) is established, we co-stained cross-sections of adult testes with our custom anti-K49ac antibody and the acrosomal marker PNA-lectin to stage tubules (Fig. 1c), and found that K49ac staining was initiated in stages VIII–IX (containing early elongating spermatids) and peaked at stages X–XI (100% of tubules) but then diminished in stages XII–VII (late-stage spermatids, Fig. 1c,d).

To examine whether P1(K49ac) is established in the cytoplasm or the nucleus, we generated a mouse line in which the endogenous P1 locus is tagged with an amino-terminal V5 tag (V5-P1). The tag has no effects on fertility or semen parameters (Extended Data Fig. 1e) and is specific to $P1^{V5/+}$ animals (Extended Data Fig. 1f). We then synchronized spermatogenesis[45,46] (Methods), collected testes enriched for stage VIII–X elongating spermatids (23 and 24 days after retinoic acid injection (Extended Data Fig. 1d)), and performed subcellular and high-salt chromatin fractionation to separate cytoplasmic proteins and chromatin-associated proteins. When we assessed lysates with anti-P1(K49ac) and anti-V5 (total P1), we detected P1 protein in both the cytoplasm and the chromatin-bound fraction (Extended Data Fig. 1g). However, P1(K49ac) is present in only the nuclear fraction and appears to have lower affinity to DNA than does unmodified P1 (Extended Data Fig. 1g,h). Despite the diminished fluorescent signal for P1(K49ac) in later stages of spermatids, P1(K49ac) was detected in elongating spermatids and sperm lysates from the epididymis and vas deferens by immunoblotting (Fig. 1e).

Fig. 1 | P1(K49ac) is acquired in the spermatid nucleus in a stage-specific manner and persists in mature mouse sperm. a, Schematic representation of modifications identified in the present study or by Brunner et al.[38] on mouse P1. **b**, Phylogenetic tree across the orders Rodentia, Primate, and Artiodactyla, using the WAG substitution strategy. Bootstrap support with 1,000 replicates is shown for each node, with values >95 indicating strong support. S9 is highlighted across species in blue and K49 is highlighted across rodents in green and in gray across more distant species that occupy alternative residues at this site. **c**, Immunofluorescence staining of P1(K49ac) in adult testes cross-sections at various seminiferous tubule stages, using PNA-lectin as the acrosomal marker. Representative images from $n = 2$ mice per time point. Scale bar, 20 µm. **d**, Quantification of P1(K49ac) stage specificity across all stages of the seminiferous epithelial cycle in adult males, highlighting specificity to late-stage VIII–XI tubules. A total of $n = 438$ tubules were counted across all stages from a total of $n = 4$ mice. **e**, Immunoblot of P1(K49ac) from elongating spermatid-enriched testes lysate, mature sperm from the epididymis, and mature sperm from the vas deferens highlights the persistence of the acetylation mark into mature sperm. Shown is a representative blot, and the experiment was repeated $n = 3$ independent times with similar results.

https://doi.org/10.1038/s41594-023-01033-4

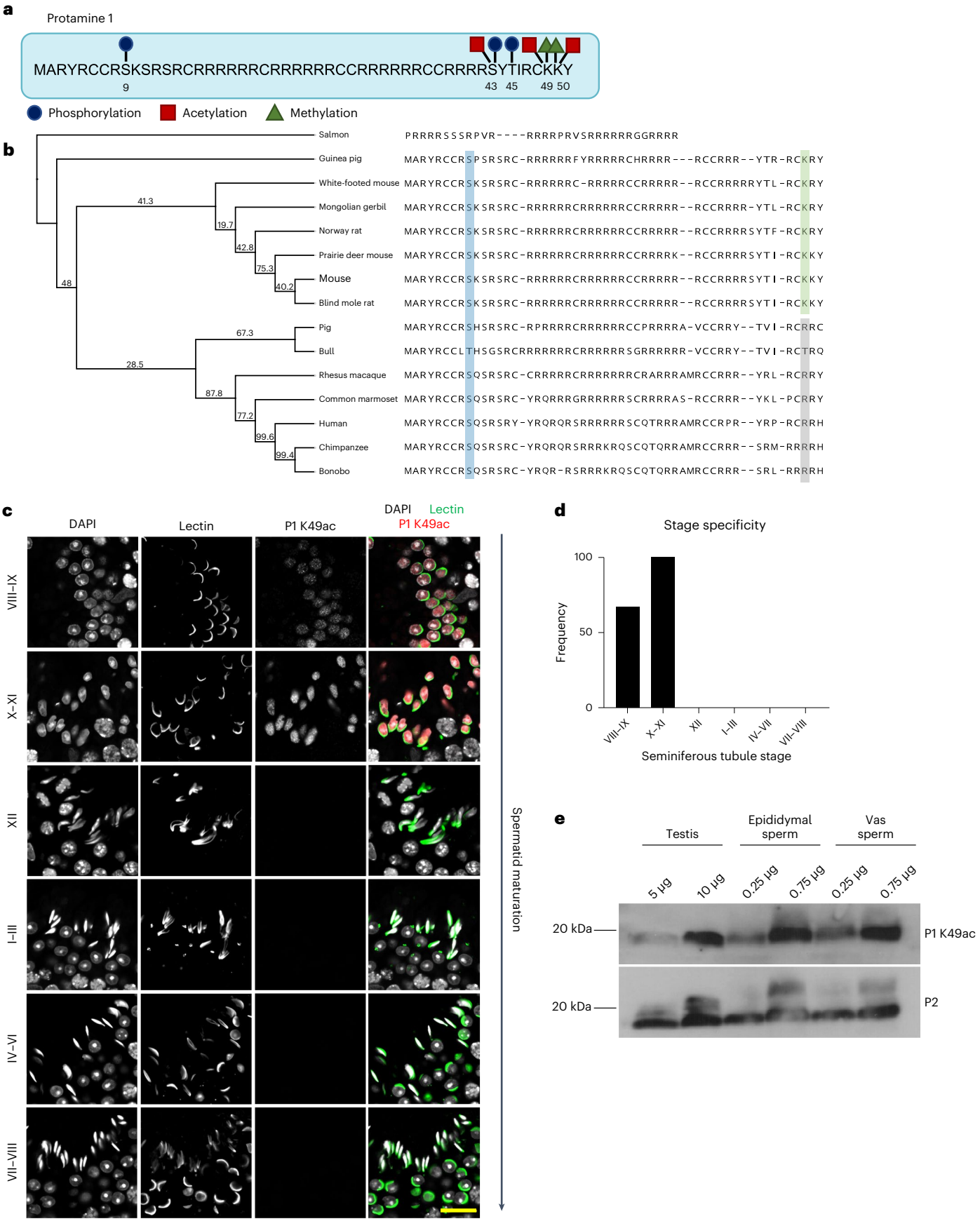

https://doi.org/10.1038/s41594-023-01033-4

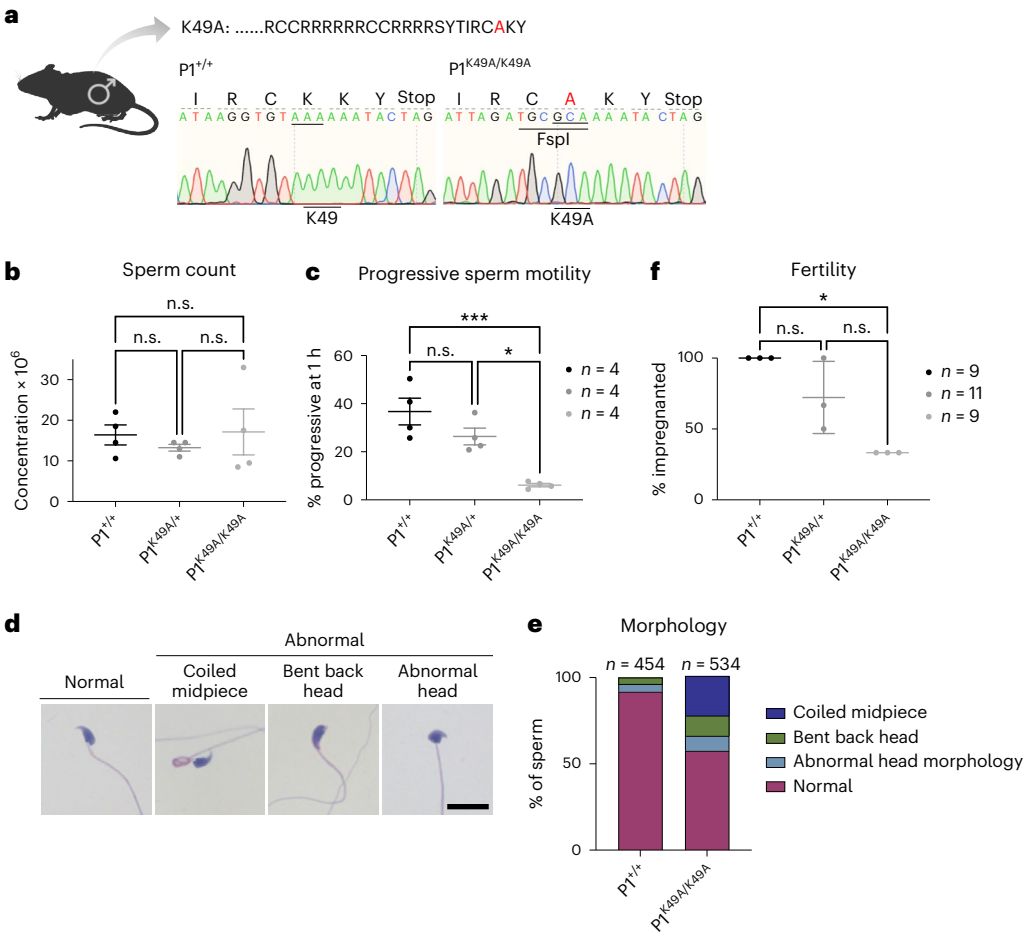

Fig. 2 | P1(K49A) results in sperm motility defects and subfertility. **a**, Schematic of the modification made to the mouse P1 sequence and corresponding Sanger sequencing traces illustrating successful mutation of K49 to alanine. A few synonymous alterations were incorporated into the donor DNA to introduce an FspI site for genotyping purposes. **b**, Total epididymal sperm count ($n = 4$ males for each genotype). Each dot represents measurement from a single animal. Statistical tests were performed using a one-way analysis of variance (ANOVA) and adjusted for multiple comparisons. The center line represents the mean, and error bars represent the s.d. **c**, Epididymal sperm progressive motility after 1 h of incubation at 37 °C; $n = 4$ males for each genotype. Each dot represents a measurement from a single animal. Statistical tests were performed using a one-way ANOVA and adjusted for multiple comparisons; $P = 0.0008$ between $P1^{+/+}$ and $P1^{K49A/K49A}$ and $P = 0.0113$ between $P1^{K49A/+}$ and $P1^{K49A/K49A}$. The center line represents the mean, and error bars represent the s.d. **d**, Representative mature sperm, stained with hematoxylin and eosin, from a $P1^{K49A/K49A}$ adult male, highlighting major abnormalities. Scale bar, 20 µm. **e**, Quantification of major abnormalities observed in $P1^{+/+}$ and $P1^{K49A/K49A}$ mature sperm. Sperm was assessed from $n = 2$ $P1^{+/+}$ males and $n = 3$ $P1^{K49A/K49A}$ males. **f**, Fertility assessment of $n = 3$ adult males per genotype, as measured by percentage of females impregnated ($n = 3$ females per male). Each dot represents measurement from a single animal. Statistical testing was performed using a Kruskal–Wallis test and with adjustment for multiple comparisons; $P = 0.0266$. The center line represents the mean, and error bars represent the s.d. n.s., not significant.

Substitution of P1 Lys49 for alanine causes sperm defects

To investigate the functional significance of P1(K49ac) in vivo, we used CRISPR–Cas9 to generate a lysine-to-alanine mutant mouse (K49A) in which we confirmed the presence of the target substitution (Fig. 2a) and absence of potential off-target modifications (Extended Data Fig. 2a). Overall, the testis in $P1^{K49A/+}$ and in $P1^{K49A/K49A}$ mice appeared phenotypically normal, with no significant differences in weight, germ cell populations detected, or sperm counts (Fig. 2b and Extended Data Fig. 2b,c). However, we observed severe subfertility, impaired progressive sperm motility (the ability of sperm to swim forward) (Fig. 2c, f), and sperm structural abnormalities, including coiled midpieces, bent back heads, and abnormal head morphology, in $P1^{K49A/K49A}$ mice (Fig. 2d, e). Importantly, P1 protein levels were comparable between genotypes (Extended Data Fig. 2d and Fig. 3a), suggesting that the phenotype is not simply due to loss of P1 protein.

P1(K49A) mutants exhibit abnormal histone retention

Next, we analyzed the effects of the K49A substitution on the histone-to-protamine exchange and mature sperm chromatin composition. When we compared protamine levels and ratios in a fixed number of sperm across genotypes, we found that ratios in $P1^{K49A/K49A}$ sperm shifted from the expected 1:2 P1:P2 ratio to a ratio closer to 1:1, owing to accumulation of unprocessed P2 (pro P2, Fig. 3a); however, total P2 levels (processed and unprocessed) remained unchanged, suggesting that the K49A substitution in P1 affects the amount of processed P2 in sperm, but not P1 or P2 expression or overall protamine levels.

As determined using both immunoblotting and quantitative mass spectrometry (MS), levels of histones in $P1^{K49A/K49A}$ sperm were ~2.5-fold higher than in $P1^{+/+}$ sperm (Fig. 3b, Extended Data Fig. 3a, b, and Supplementary Table 2), suggesting that overall histone eviction was disrupted. As H4 hyperacetylation is indispensable for histone-to-protamine exchange[8,47–50], we next analyzed $P1^{+/+}$ and $P1^{K49A/K49A}$ testes using an anti-H4 tetra-acetyl (referred to as ac-H4) antibody, but observed no significant difference in ac-H4 levels by immunostaining or immunoblotting (Fig. 3c and Extended Data Fig. 3c) or by quantitative MS (Extended Data Fig. 3d). Similarly, in both testis cross-sections subjected to immunostaining and testes lysates

subjected to immunoblotting, we did not find any changes in transition proteins (TNP1 and TNP2), which are well-known chromatin intermediate components of the histone-to-protamine exchange whose loss perturbs sperm morphology, chromatin composition, and final chromatin packaging—similar to our observations in $P1^{K49A/K49A}$ mice (Fig. 3c and Extended Data Fig. 3c,e). Thus, in spite of abnormal chromatin packaging, the $P1^{K49A/K49A}$ mutants appear to progress normally through several key intermediate processes.

P1(K49A) mutant sperm lack well-defined histone positioning

To better understand where nucleosomes are retained along the genome in $P1^{K49A/K49A}$ mutant sperm, we performed micrococcal nuclease digestion followed by sequencing (MNase-seq) of chromatin from four $P1^{+/+}$ and two $P1^{K49A/K49A}$ sperm samples (Extended Data Fig. 3f)[51]. As expected, nucleosomes in wild-type (WT) sperm were enriched at transcription start sites (TSSs) of key developmental loci (*Hoxd*, *Dux*, *Nanog*, and *Pou5f1*) and imprinted genes (for example, *Mest, Igf2os*, and *Snrpn*), but less so at introns and distal intergenic regions (Fig. 3d–f, Extended Data Fig. 4a–d, and Supplementary Table 3)[52–55].

On the basis of a 5% false-discovery rate (FDR) cut-off, $P1^{K49A/K49A}$ mutant sperm maintain only ~3% of the peaks found in wild-type sperm, despite having overall higher histone retention (Extended Data Fig. 3g and Supplementary Table 4). However, the majority of nucleosome peaks detected in wild-type sperm are maintained at low levels of enrichment in mutant sperm (Fig. 3d–g and Extended Data Fig. 3h), indicating that histone retention profiles are less defined or fixed in mutant sperm (*Hoxd* cluster, *Dux*, and *Pou5f1*; Extended Data Fig. 4a–d). Although the majority of enriched peaks in mutant sperm have a high degree of overlap with wild-type sperm (66.5%), novel peaks were acquired at ectopic sites (~400). A smaller percentage of ectopic peaks were enriched at promoters, but a greater fraction mapped to introns and distal intergenic regions (Fig. 3f,g). Given that nucleosomes in sperm tend to be over-represented in CpG-rich regions, we next examined whether wild-type, shared, or mutant-only peaks preserved this histone-retention property. We found that mutant mice were unique in having largely lost enrichment at high-GC-content regions (Fig. 3h).

P1(K49A) sperm retain differentially modified histones

Given the differences in histone retention patterns in $P1^{+/+}$ and $P1^{K49A/K49A}$ sperm, we next performed bottom-up mass spectrometry on acid-extracted histones from $P1^{+/+}$ or $P1^{K49A/K49A}$ sperm to investigate potential differences in histone modification states (Extended Data Fig. 4e,f and Supplementary Table 5). Of ~80 modified states, $P1^{K49A/K49A}$ sperm maintained an increased level of dimethylated histone H3 R42 (H3R42me2) compared with that in $P1^{+/+}$ sperm. This modification has previously been shown to induce nucleosome destabilization and stimulate transcription in vitro[56], but testing this model in the context of the P1(K49A) substitution is challenging owing to difficulty in generating specific antibodies[56]. Additionally, we found that modifications of H3.3 were unaffected, but that H3K27me3, H3K36me2, and H3K36me3 on H3.1 were increased in $P1^{K49A/K49A}$ sperm, suggesting possible differences in the ability of P1(K49A) (either indirectly or directly) to evict stable nucleosomes such as the H3.1-containing nucleosome, leading to possible accumulation of H3.1-containing nucleosomes (along with associated modifications) (Extended Data Fig. 4f).

P1 DNA-binding ability varies with DNA fragment length

Assessing how protamine–DNA binding or dynamics are regulated in the testis in vivo remains technically challenging; therefore, we employed bulk biochemical and single-molecule assays in vitro to examine protamine–DNA interactions. To overcome challenges associated with generating recombinant P1 and P2 proteins in bacteria owing to their high arginine content, we developed an acid extraction and size-exclusion chromatography method to purify P1 and P2 proteins (amino acid sequences shown in Fig. 4a) from both $P1^{+/+}$ (referred to as wild-type (WT) P1 or P2) and $P1^{K49A/K49A}$ mature sperm (referred to as P1(K49A) or pro P2) (Fig. 4b). Our method allowed separation of P1 and P2 from not only each other, but also other basic proteins such as histones (Extended Data Fig. 5a,b).

To test the binding affinity of wild-type P1 or P1(K49A) to DNA of various lengths, we used a combination of fluorescence anisotropy and electrophoretic mobility-shift assays (EMSAs). Using a 99-base-pair (bp) fluorescein-labeled DNA fragment for anisotropy, we found that wild-type P1 robustly bound DNA in a concentration-dependent manner, with an apparent binding affinity ($K_{d,app}$) of 0.47 µM. Similarly, P1(K49A) had a $K_{d,app}$ of 0.46 µM, suggesting that there is no difference in DNA-binding ability with a short DNA fragment (Fig. 4c). However, binding efficiencies differed when P2 proteoforms were compared: mature P2 bound DNA more efficiently than did pro P2 ($K_{d,app}$, 0.35 µM versus 0.56 µM; Fig. 4d).

Next, we turned to EMSAs to examine binding to DNA fragments of increasing length. Using a 300-bp fragment, we found that, after 1 h, wild-type P1 bound DNA in a concentration-dependent manner, whereas binding affinity was slightly decreased for P1(K49A) ($K_{d,app}$, 0.95 µM versus 0.68 µM) (Fig. 4e,f). Because the protamine–DNA complex does not enter the gel, we inferred that protamine–DNA complexes form large, higher-order structures that preclude migration into the gel. Consistently, in EMSA experiments in the presence of proteinase K, DNA movement into the gel resumed, suggesting that the well shift is representative of protamine–DNA interactions and not a technical artifact (Extended Data Fig. 5c). Interestingly, both P1 and P1(K49A) appeared to be capable of cooperative binding behavior on a 300-bp fragment, as evidenced by their Hill coefficients of >1 (for wild-type P1 and P1(K49A): 4.2 versus 3.0, with comparable data for wild-type P2 and pro P2: 4.2 versus 3.7) (Fig. 4g,h), and similarly, neither binding affinity was affected by incubation time (Extended Data Fig. 5d–g).

Since mouse sperm (and most mammalian sperm) use both P1 and P2 to package chromatin, we next asked how the presence of both proteins influences affinity to DNA, and whether the P1(K49A) substitution alters this affinity. Thus, we repeated EMSAs using wild-type P1 or P1(K49A) in combination with either wild-type P2 or pro P2 in a 1:2 ratio. The combination of wild-type P1 andP2 bound more efficiently

Fig. 3 | P1(K49A) substitution alters sperm chromatin composition. a, Acid urea gel electrophoresis of sperm basic proteins reveals a shift in P1:P2 ratio in $P1^{K49A/K49A}$ males by Coomassie blue staining (top). Immunoblotting reveals no difference in P1 level but an accumulation of pro P2 (bottom panels). P1:P2 ratios, as quantified in ImageJ, are displayed below the immunoblot. **b**, Quantification of retained histone H3 (top) and histone H2B (bottom) in $P1^{+/+}$ or $P1^{K49A/K49A}$ sperm, as determined by quantitative bottom-up MS. Statistical analyses were performed using a nested, two-tailed *t*-test, $P = 0.0543$ for H3 and $P = 0.0221$ for H2B. The center line represents the mean, and error bars represent the s.d. Each dot represents the average of three technical replicate measurements for a single biological replicate ($n = 3$ biological replicates per genotype). **c**, Immunofluorescence staining of adult $P1^{+/+}$ or $P1^{K49A/K49A}$ testes cross-sections for ac-H4 (left panels) or TNP2 (right panels). Scale bar, 20 µm. Shown are representative images, and similar results were obtained from $n = 3$ independent males. **d**, Heatmap showing enrichment of genome-wide MNase-seq signal ±2.5 kb from the TSS (bottom) and corresponding enrichment profiles (top). Units next to the color bars indicate normalized fold enrichment. **e**, Heatmap showing enrichment of MNase-seq signal around regions called as peaks in both WT and mutant ±2.5 kb from the peak center (bottom), and corresponding enrichment profiles (top). Units next to the color bars indicate normalized fold enrichment. **f**, Bar plot depicting enrichment of nucleosome peaks in either $P1^{+/+}$ or $P1^{K49A/K49A}$ sperm across various genomic features. **g**, Venn diagram of overlapped MNase-seq peaks (FDR ≥ 5%) between wild-type (WT) and mutant sperm. **h**, GC percentage of nucleotide sequences at peaks in WT and mutant sperm.

https://doi.org/10.1038/s41594-023-01033-4

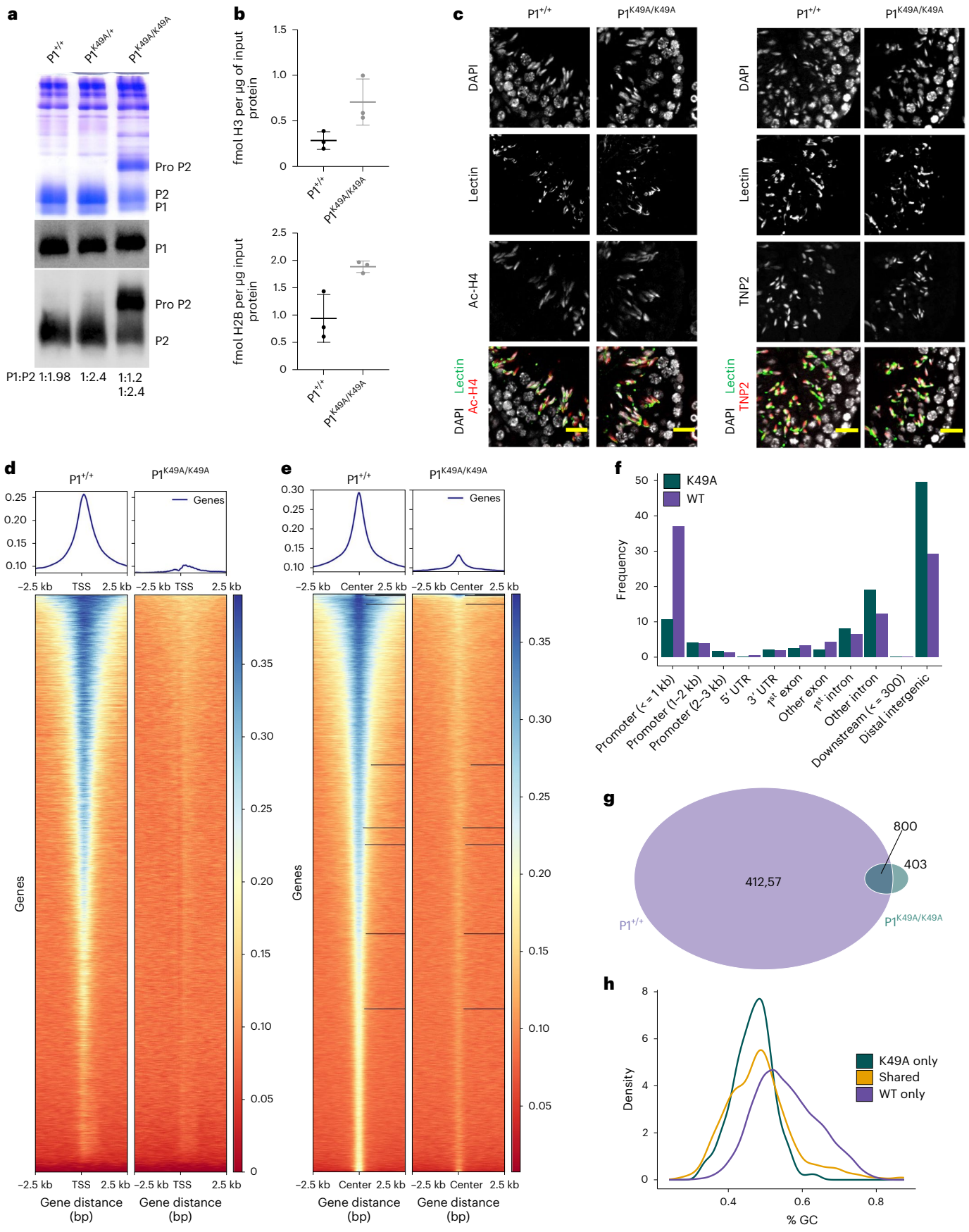

https://doi.org/10.1038/s41594-023-01033-4

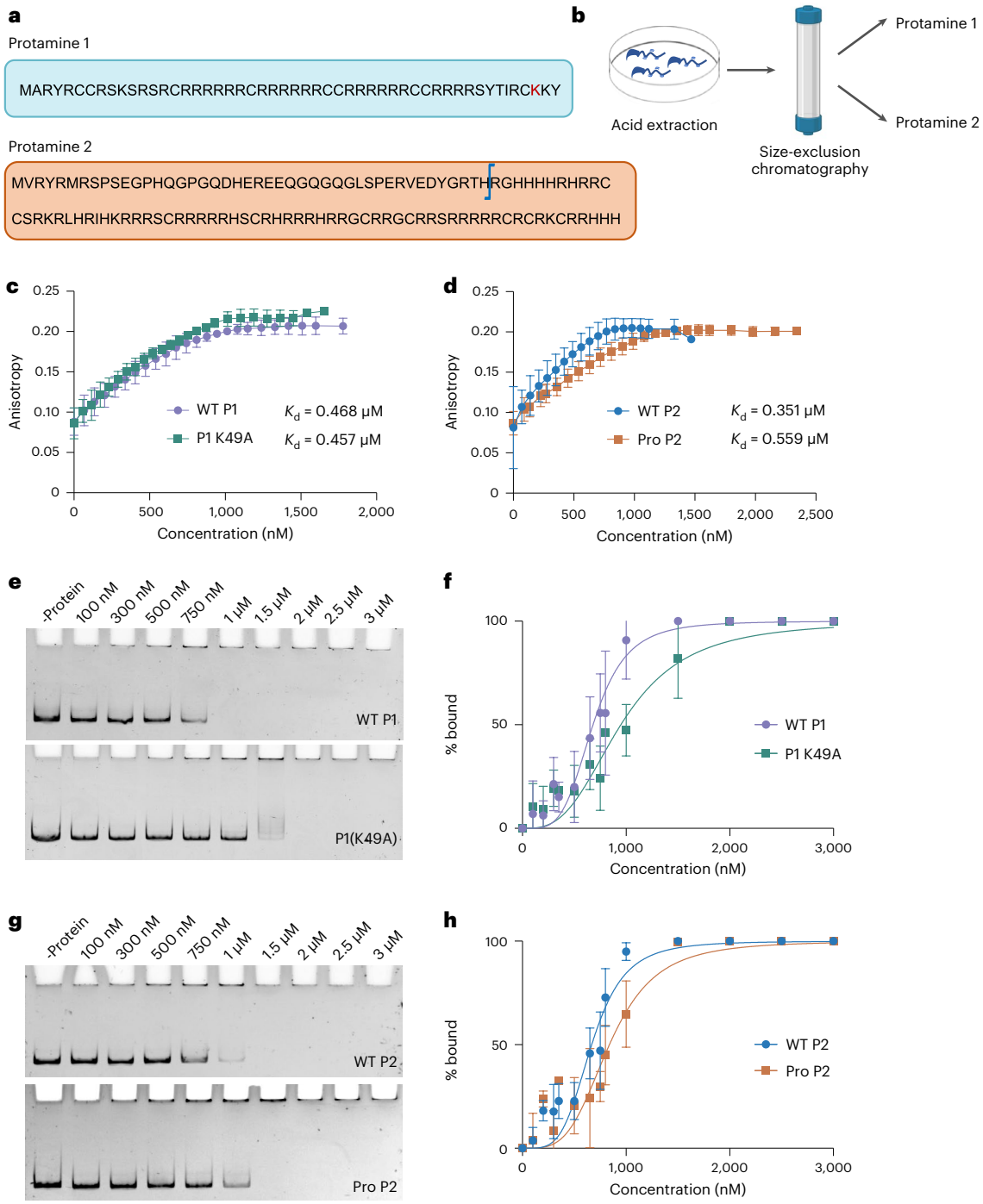

Fig. 4 | Protamine–DNA binding ability varies with DNA length. a, Schematic of mouse P1 and P2 sequences. Blue bar in P2 indicates cleavage site. **b**, Scheme for purifying P1 and P2 from mature mouse sperm. **c**,**d**, Quantification of the binding affinities of wild-type (WT) P1 and P1(K49A) (**c**) or WT P2 and pro P2 (**d**) to a linear 99-bp 5′-FAM labeled DNA fragment using fluorescence anisotropy. $K_{d,app}$ values were calculated using the Hill equation and were taken from $n = 3$ biologically independent samples per protein over 3 independent experiments. For each time point of each independent experiment, a total of 22 replicate measurements were averaged. Error bars represent s.e.m. **e**, Representative EMSAs of a titration of increasing amounts of WT P1 (top) or P1(K49A) (bottom) illustrating their interaction with a ~300 bp DNA fragment. **f**, Quantification of the binding affinities of WT P1 and P1(K49A) to a linear ~300-bp DNA fragment, determined by EMSA. $K_{d,app}$ values were calculated using the Hill equation and are presented as an average of $n = 8$ technical replicates across $n = 3$ biologically independent samples for WT P1 and $n = 9$ technical replicates across $n = 3$ biologically independent samples for P1(K49A). Error bars represent s.d. **g**, Representative EMSAs of a titration of increasing amounts of WT P2 (top) or pro P2 (bottom) illustrating their interaction with a ~300-bp DNA fragment. **h**, Quantification of the binding affinities of WT P2 and pro P2 to a linear ~300-bp DNA fragment determined by EMSA. $K_{d,app}$ values were calculated using the Hill equation and are presented as an average of $n = 9$ technical replicates across $n = 3$ biologically independent samples for WT P2 and $n = 8$ technical replicates across $n = 3$ biologically independent samples for pro P2. Error bars represent s.d.

to DNA than did either protein alone, but upon mixing wild-type P1 with pro P2, affinity decreased substantially (Extended Data Fig. 5h,i). Although binding properties of P1(K49A) with either wild-type P2 or pro P2 appear identical, both conditions require a higher protein concentration (~1.2 μM of total protamine) to reach a fully bound state (Extended Data Fig. 5h,i).

Taken together, our results show that on short DNA fragments, binding affinities between wild-type P1 and P1(K49A) are indistinguishable, whereas the binding affinity of pro P2 is markedly reduced compared with that of wild-type P2. On longer DNA fragments, P1(K49A) maintains a cooperative binding mode, but DNA binding affinity is decreased. Furthermore, we show that protamine–DNA binding affinity and cooperative behavior are enhanced in the presence of both P1 and P2, but that mutant P1 loses its preferred selectivity for mature P2.

P1(K49A) protein exhibits altered DNA compaction kinetics

EMSAs measure the equilibrium between on rate (k_{on}) and off rate (k_{off}), but not kinetics. Hence, we turned to DNA curtain assays to investigate real-time compaction and decompaction of bacteriophage λ DNA (λ-DNA) in the presence of wild-type and mutant protamines at single-molecule resolution (Fig. 5a). Protamines are expected to bind to 10- to 15-bp sites[57], and the 50 kb of λ-DNA contains a large diversity of 10- to 15-bp sites that occur frequently within the mouse genome, allowing assessment of representative protamine–DNA interactions. To investigate these interactions, we labeled each λ-DNA molecule with a fluorescent dCas9 at the untethered end and monitored changes in DNA length (Fig. 5b).

Wild-type P1 largely failed to initiate compaction at a concentration of 100 nM, but induced robust and complete DNA compaction at a 200 nM concentration, with an average velocity of 1.57 μm s^{-1} (~6 kbp s^{-1}) (Fig. 5c,e,g). At the same concentration, P1(K49A) failed to initiate compaction, but achieved robust compaction at a 275 nM concentration (Fig. 5d,f,g). The average velocity for P1(K49A) at the concentration necessary for full compaction was also slower than that of wild-type P1 (1.09 μm s^{-1} at 275 nM versus 1.57 μm s^{-1} at 200 nM). Notably, at a low protein concentration, and for both wild-type P1 and P1(K49A), only a few molecules condensed >10 kilobases of DNA (Fig. 5g), whereas most DNA molecules remained uncompacted, with a few strands initiating compaction stochastically. At intermediate protein concentrations (P1: 125–175 nM, P1(K49A): 225–250 nM), the extent of DNA compaction was non-uniform (Fig. 5g); that is, DNA compaction exhibited a start-and-stop behavior, and not all strands within a single experiment experienced the same level of compaction (Fig. 5c,d,g). Furthermore, even directly adjacent DNA molecules, separated by only a couple micrometers, did not exhibit the same behavior (that is, the neighboring DNA molecule could become completely compacted or not at all compacted; Fig. 5h). On the basis of these data, we conclude that protamines, when present in limited amounts, preferentially bind cooperatively to a small number of DNA molecules, as opposed to generating a uniform but low level of compaction across all available DNA molecules.

Next, we assessed the compaction kinetics of wild-type P2 and pro P2 on DNA curtains. Pro P2 initially binds to DNA in elongating spermatids and then undergoes proteolytic cleavage to generate mature wild-type P2. Wild-type P2 required a 250 nM concentration to achieve robust compaction (similar to P1(K49A))—roughly 22% more protein than wild-type P1. The compaction rate for P2 was faster than it was for wild-type P1 or P1(K49A) (2.01 μm s^{-1} versus 1.57 μm s^{-1} for P1(K49A); Fig. 5f and Extended Data Fig. 6c), suggesting that P2 has a lower binding affinity or a higher nucleation barrier to form filaments on DNA, but stronger cooperative behavior, than does wild-type or mutant P1. Unlike mature P2, pro P2 has a lower affinity to DNA and compacts DNA at a slower rate (1.26 μm s^{-1} versus 1.97 μm s^{-1} for wild-type P2; Extended Data Fig. 6b,d,e), and the extent of compaction generated by wild-type P2 is much greater (for example, ~9 μm for wild-type P2 and ~4 μm for pro P2 after 5 s at 275 nM), consistent with increased genome compaction after P2 processing (Extended Data Fig. 6c,d).

DNA initially condensed by P1(K49A) decompacted faster than DNA bound by wild-type P1 (0.97 μm min^{-1}, ~3.6 kb min^{-1} versus 0.45 μm min^{-1}, ~1.7 kbp min^{-1}) (Fig. 5i). Likewise, pro-P2-compacted DNA decompacted faster than DNA stably compacted by wild-type P2 (0.45 μm min^{-1}, ~1.7 kb min^{-1} versus 0.37 μm min^{-1}, ~1.4 kb min^{-1}) (Extended Data Fig. 5f). Together, these data suggest that P2 binds weakly to DNA at low protein concentrations and requires a large amount of protein to achieve compaction, but above its threshold, it achieves fast compaction, a significantly different behavior than what was observed for wild-type P1, which binds DNA efficiently at intermediate concentrations and is less sensitive to small concentration changes. We surmise that these opposing characteristics of DNA compaction and decompaction are central to the opposing roles of protamines in sperm versus zygotes.

Consistent with bulk $K_{d,app}$ measurements, mutant P1 compacts DNA at a slower rate but dissociates from DNA faster, whereas wild-type P2 (relative to pro P2) requires more protein to initiate compaction but compacts DNA at a faster rate and to a greater extent, and dissociates slower. Moreover, P1(K49A)-compacted DNA decompacts substantially faster than does DNA compacted by wild-type P1, explaining our observation in embryos described below. Therefore, although electrostatics drive sperm DNA condensation, PTMs or individual residues fine-tune DNA compaction and decompaction to ensure that packaging is coupled with key developmental events.

P1(K49A) substitution accelerates paternal DNA decompaction

Given reduced sperm motility and subfertility in $P1^{K49A/K49A}$ males, we performed intracytoplasmic sperm injection (ICSI) to examine how the P1(K49A) substitution impacts early embryonic development. We found that blastocyst formation was significantly impaired (27% versus 63% blastocysts formed upon injection of $P1^{K49A/K49A}$ versus $P1^{+/+}$ sperm) (Supplementary Table 6), and we identified the one-cell to two-cell transition and, surprisingly, the morula-to-blastocyst transition as two critical developmental barriers in embryos derived from $P1^{K49A/K49A}$ sperm (Supplementary Table 6), suggestive of abnormal developmental programming in mutant embryos.

Since proper decompaction of the paternal genome is critical for embryonic development following fertilization, we next examined the protamine-to-histone exchange process and whether early embryonic processes occur normally in zygotes derived from $P1^{K49A/K49A}$ sperm. By DAPI staining of zygotes (collected 4 h post-fertilization (hpf); Fig. 6a), we found that the average relative male pronuclear size (male/female)

Fig. 5 | P1(K49A) substitution alters DNA compaction and decompaction kinetics in vitro. a, Schematic of DNA curtains. DNA molecules are labeled at the 3′ end by dCas9 (shown in pink). **b**, Cartoon representation shown aside actual images of protamine-driven DNA compaction. **c**,**d**, Representative kymographs of DNA compaction induced by WT P1 (**c**) or P1(K49A) (**d**) at increasing protein concentrations. **e**, Average DNA compaction by WT P1 at increasing concentrations. Error bars represent s.d. (n = 78 traces for 100 nM, n = 67 for 125 nM, n = 78 for 150 nM, n = 63 for 175 nM, and n = 66 for 200 nM). **f**, Average DNA compaction by P1(K49A) at increasing concentrations. Error bars represent s.d. (n = 48 traces for 200 nM, n = 74 for 225 nM, n = 68 for 250 nM, and n = 81 for 275 nM). **g**, Traces of individually tracked DNA molecules over time at a low, intermediate, or high concentration of either WT P1 (left panels) or P1(K49A) (right panels), illustrating cooperative behavior. **h**, Representative image of WT P1-driven compaction of adjacent DNA molecules within the curtain, highlighting differences in compaction even between DNA molecules that are beside each other. **i**, Decompaction of DNA initially compacted by WT P1 and P1(K49A) over time illustrates differences in decompaction rates. Data were collected from n = 3 independent experiments (n = 3 flow cells per experiment) for each protein. A total of n = 142 single DNA molecules were measured for WT P1 and n = 133 single DNA molecules were measured for P1(K49A). Error bars represent s.e.m.

https://doi.org/10.1038/s41594-023-01033-4

in zygotes derived from P1$^{K49A/K49A}$ sperm was significantly larger than in zygotes derived from P1$^{+/+}$ sperm, suggesting accelerated decompaction of paternal chromatin (Fig. 6b), consistent with our DNA curtain experiments.

P1(K49A) embryos have altered DNA replication patterns

During the first embryonic cell cycle, DNA replication initiates synchronously in both pronuclei, but progresses asynchronously such that the male pronucleus completes replication before the female

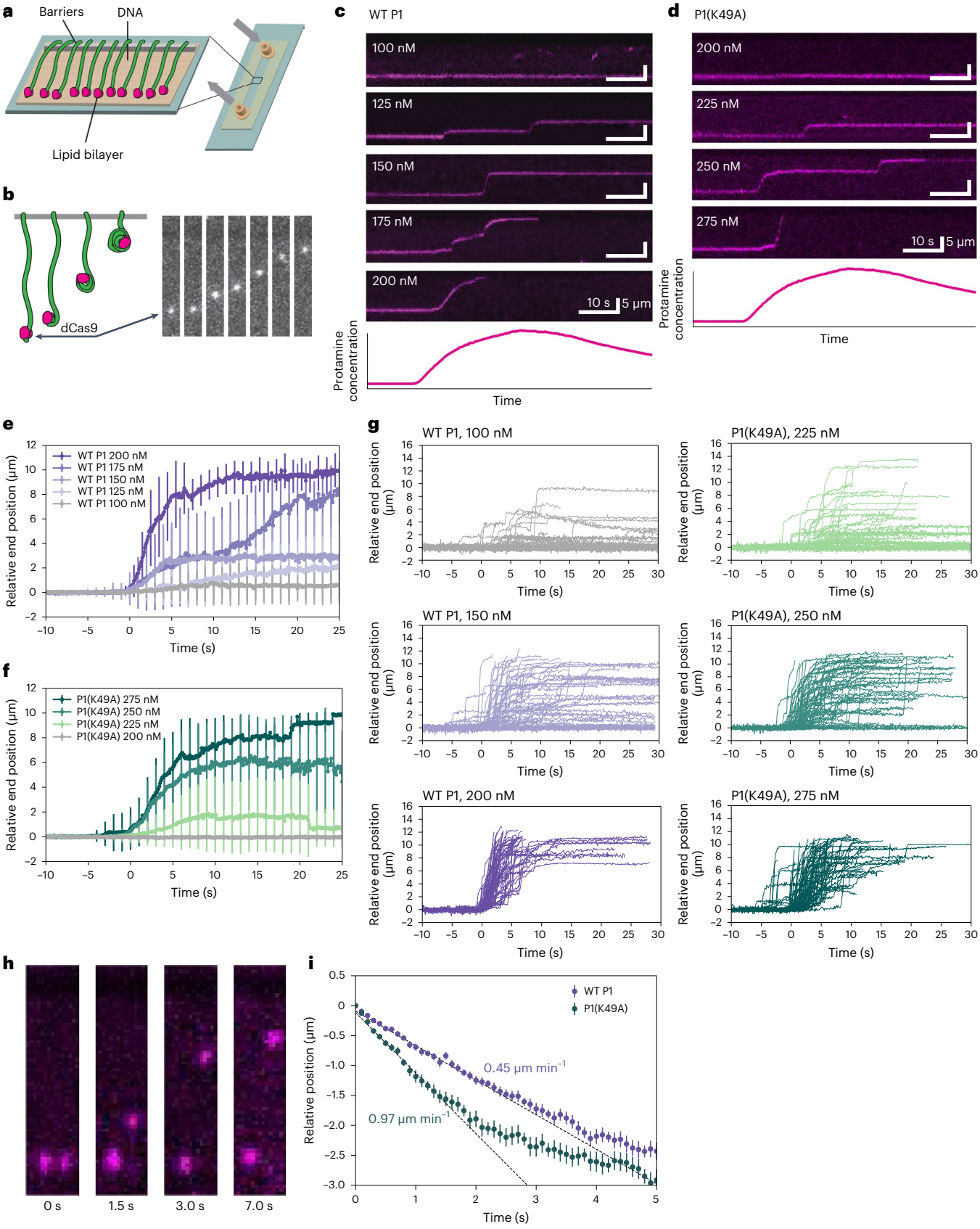

pronucleus[58]. In euchromatic regions, replication is detected as diffuse BrdU staining (cartoon schematic group I, Extended Data Fig. 7a), which progresses to heterochromatic regions, appearing as ring-like patterns corresponding to perinuclear and perinucleolar heterochromatin (cartoon schematic groups II–IV, Extended Data Fig. 7a). Although mutant embryos typically follow normal DNA replication patterns (Extended Data Fig. 7b), the proportions of embryos differ such that 63% of wild-type embryos replicated heterochromatic regions exclusively (groups III–IV), whereas ~64% of mutant embryos replicated primarily euchromatic regions (groups I and II, Extended Data Fig. 7c). Furthermore, in ~20% of mutant embryos, the DNA replication pattern was altered in parental pronuclei such that the paternal genome replicated euchromatin while the maternal genome replicated perinucleolar heterochromatin ('other' category, Extended Data Fig. 7c,d).

Consistent with temporal differences in DNA replication, BrdU fluorescence intensity was higher in late-replicating mutant embryos, suggesting that replication may be delayed or stalled in mutants relative to wild-type embryos (Extended Data Fig. 7e). Changes in DNA replication kinetics in embryos or somatic cells were previously shown to be associated with elevated DNA damage and altered chromosome segregation, leading to aneuploidy[59–62]. Here, we find that mutant two-cell embryos had higher DNA damage levels, as determined by increased γ-H2Ax fluorescence intensity (Fig. 6c). Furthermore, multiple nuclei or micronuclei were present in mutant embryos, indicating chromosome segregation abnormalities[63] (Extended Data Fig. 7f). Altogether, these observations suggest that controlled remodeling or protamine removal from the paternal genome may be critical for coordinating DNA replication dynamics between pronuclei and downstream chromosome segregation and developmental programming.

Mutant two-cell embryos display differences in gene expression

We next examined whether changes in DNA replication kinetics affected zygotic genome activation (ZGA). Thus, we treated wild-type and mutant two-cell ICSI embryos (collected 24–30 h post-injection, hpi) with the uridine analog EU 30 min prior to collection. EU fluorescence intensity in mutant embryos was variable, but ~2.5-fold higher than in wild-type embryos (Fig. 6d), consistent with earlier data showing that interfering with DNA replication in early two-cell embryos increases EU incorporation[64]. We then performed RNA-sequencing analysis on 27 post-quality-control 2-cell samples ($n = 11$ wild-type embryos and $n = 16$ K49A mutant embryos) and compared the data with a previously published mouse dataset, including zygotes, 2-cell (early-to-late stages), 4-cell, 8-cell, 16-cell embryos, and early-to-late blastocysts. Despite variability, our two-cell embryos were most similar to the published mid-to-late two-cell samples, and wild-type and K49A samples were similar to each other (Fig. 6e). Thus, the high correlation between mutant and wild-type embryos suggests that ZGA is likely not globally dysregulated in K49A mutant embryos (Fig. 6e).

Next, we performed Gene Ontology analysis of up- and downregulated genes (greater than twofold change between wild-type and mutant embryos). Downregulated genes in mutant embryos included cell cycle regulators (*Cdk1*, *Mcm4*, *Incenp*, *Sgo2a*, and *Fbxo5*), protein kinases (*Aurka*, *Aurkb*, *Dclk1*, *Pbk*, and *Dyrk44*), genes implicated in chromosome segregation (*Zscan*, *Zbtb7c*, *Sgo2a*, *Kntc1*, *Aurka*, and *Aurkb*), and DSB repair (*Msh2*, *Ercc4*, *Aunip*, *Exd2*, and *Parp9*), consistent with the altered DNA replication dynamics, elevated levels of DNA damage, and increased fraction of embryos containing micronuclei (Fig. 6c, Extended Data Fig. 7c,f, and Supplementary Table 7). Several key ZGA genes were downregulated, including *Zscan4d*, a Dux target gene exclusively expressed in late two-cell embryos (Fig. 6g–i and Extended Data Fig. 7g)[65–69]. Genes upregulated in P1(K49A) embryos were enriched for apoptosis and oxidative phosphorylation (Fig. 6g–i and Supplementary Table 7); the latter is an unexpected finding, given that oxidative phosphorylation is generally upregulated in blastocysts[70].

Thus, the single P1 amino acid substitution results in accelerated paternal chromatin decompaction and increased zygote stalling, likely initiating global dysregulation of DNA replication. While global ZGA is not severely perturbed, the expression of several key developmental genes is significantly decreased. Thus, these results confirm the functional significance of the K49 residue at the organismal level.

Defects in mutant males are not driven only by charge

The K49A substitution alters both electrostatic properties and the molecular volume of the modified residue, making it difficult to distinguish whether loss of acetylation or loss of a positive charge at the K49 site causes the observed phenotypes. To distinguish between these possibilities, we created a K49R mouse model in which the positive charge is preserved but the acetylation is eliminated (Fig. 7a). Although no overt phenotype was observed in $P1^{K49R/+}$ males, progressive sperm motility was decreased, and morphologically abnormal sperm increased in $P1^{K49R/K49R}$ males, similar to $P1^{K49A/K49A}$ males (Fig. 7b,c), suggesting that the lysine-to-arginine substitution does not rescue sperm defects observed in $P1^{K49A/K49A}$ males. While generating a K49R mutant, we generated a truncated P1 mouse model in which residues 46–51 in the C-terminus of P1 were deleted (P1(Δ46–51), Fig. 7a). The truncated P1 protein expression was stable, escaping nonsense-mediated decay (albeit RNA levels were reduced by about twofold in $P1^{\Delta46-51/+}$ and $P1^{\Delta46-51/\Delta46-51}$ testes, Fig. 7d), and is incorporated into chromatin but at lower efficiency (Fig. 7e). Notably, decreased progressive sperm motility and morphologically abnormal sperm are features of both heterozygous and homozygous P1(Δ46–51) males (Fig. 7b,c). Thus, the P1(Δ46–51) protein likely has a dominant-negative phenotype, possibly affecting P1–P1 or P1–P2 interactions. Together, these data suggest that protein sequences outside the arginine core likely confer species-specific biophysical and structural properties of protamine proteins.

Fig. 6 | The K49A substitution in P1 results in decreased blastocyst formation, accelerated decondensation of paternal chromatin, and altered gene expression. a, Experimental scheme for assessing pronuclear size. **b**, Quantification of relative male pronuclear size (male/female) in zygotes derived from either $P1^{+/+}$ or $P1^{K49A/K49A}$ sperm. Statistical testing was done using an unpaired, two-sided *t*-test, $P = 0.0075$. Quantification was performed from a total of $n = 12$ $P1^{+/+}$ zygotes and $n = 13$ $P1^{K49A/K49A}$ zygotes. The center line represents the median. **c**, Total gH2AX fluorescence intensity per blastomere in $P1^{+/+}$ and $P1^{K49A/K49A}$ two-cell embryos. Embryos containing micronuclei or multiple nuclei were not included. Measurements were taken from a total of $n = 38$ blastomeres from WT embryos and a total of $n = 10$ blastomeres from mutant embryos. Statistical testing was done using an unpaired, two-sided *t*-test, $P = 0.0023$. Center line represents the median. **d**, Total EU fluorescence intensity per blastomere in $P1^{+/+}$ and $P1^{K49A/K49A}$ two-cell embryos. Embryos containing micronuclei or multiple nuclei were not included. Measurements were taken from a total of $n = 38$ WT blastomeres and a total of $n = 10$ mutant blastomeres. Statistical testing was performed using an unpaired, two-sided *t*-test, $P = 0.0003$. The center line represents the median. **e**, Heatmap of the correlation matrix between our 27 two-cell embryos (11 WT and 16 K49A) (left to right) and an external dataset of 286 samples (top to bottom), covering multiple stages of mouse preimplantation development and showing a high degree of transcriptomic similarity of both WT and mutant embryos with previously published mid- and late-two-cell mouse embryos. Color bar represents Pearson correlation coefficient (*r*). Color range: blue-minimal correlation coefficient value of 0.141; red-maximal value of 0.701. **f**, Gene Ontology analysis of genes that are downregulated in mutant two-cell embryos compared with WT. **g**–**i**, Violin plots of individual representative genes whose expression is either unchanged (**g**), upregulated (**h**), or downregulated (**i**) in mutant two-cell embryos compared with WT embryos. Data from $n = 10$ WT embryos and $n = 13$ mutant embryos are included.

https://doi.org/10.1038/s41594-023-01033-4

Discussion

Efficient eviction of histones and protamine packaging of paternal chromatin during spermiogenesis safeguards fertility throughout life. Given the arginine-rich composition of protamines, previous work has assumed that there is a non-specific protamine–DNA binding mechanism, leaving the contribution of individual P1 or P2 residues to chromatin condensation in spermatids and unpackaging in the zygote unresolved. Here, we pioneered complementary molecular, genetic, biochemical, and biophysical assays to investigate how replacing K49 of P1 with an alanine or arginine residue systematically perturbs sperm genome packaging and early remodeling events in the zygote.

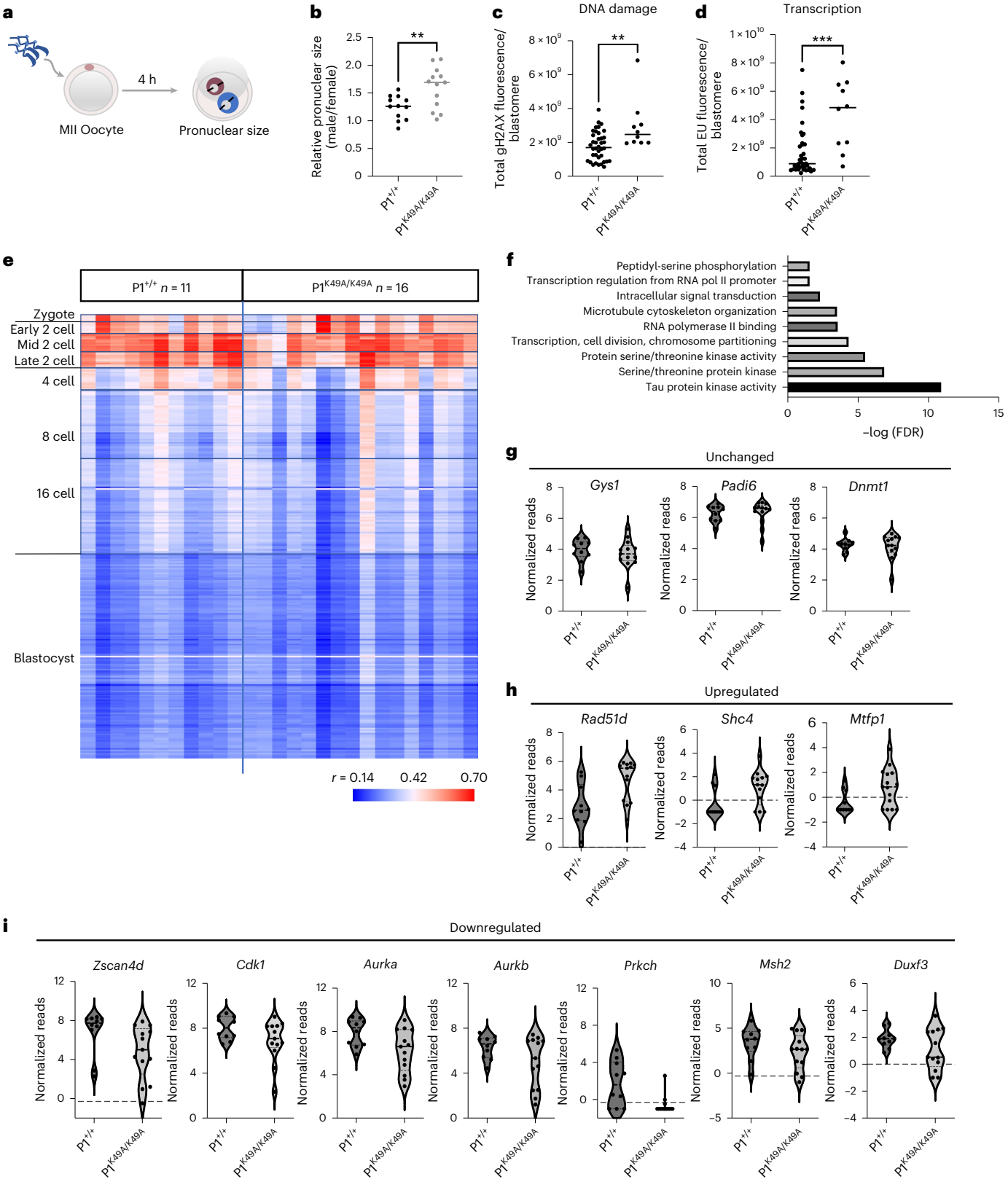

https://doi.org/10.1038/s41594-023-01033-4

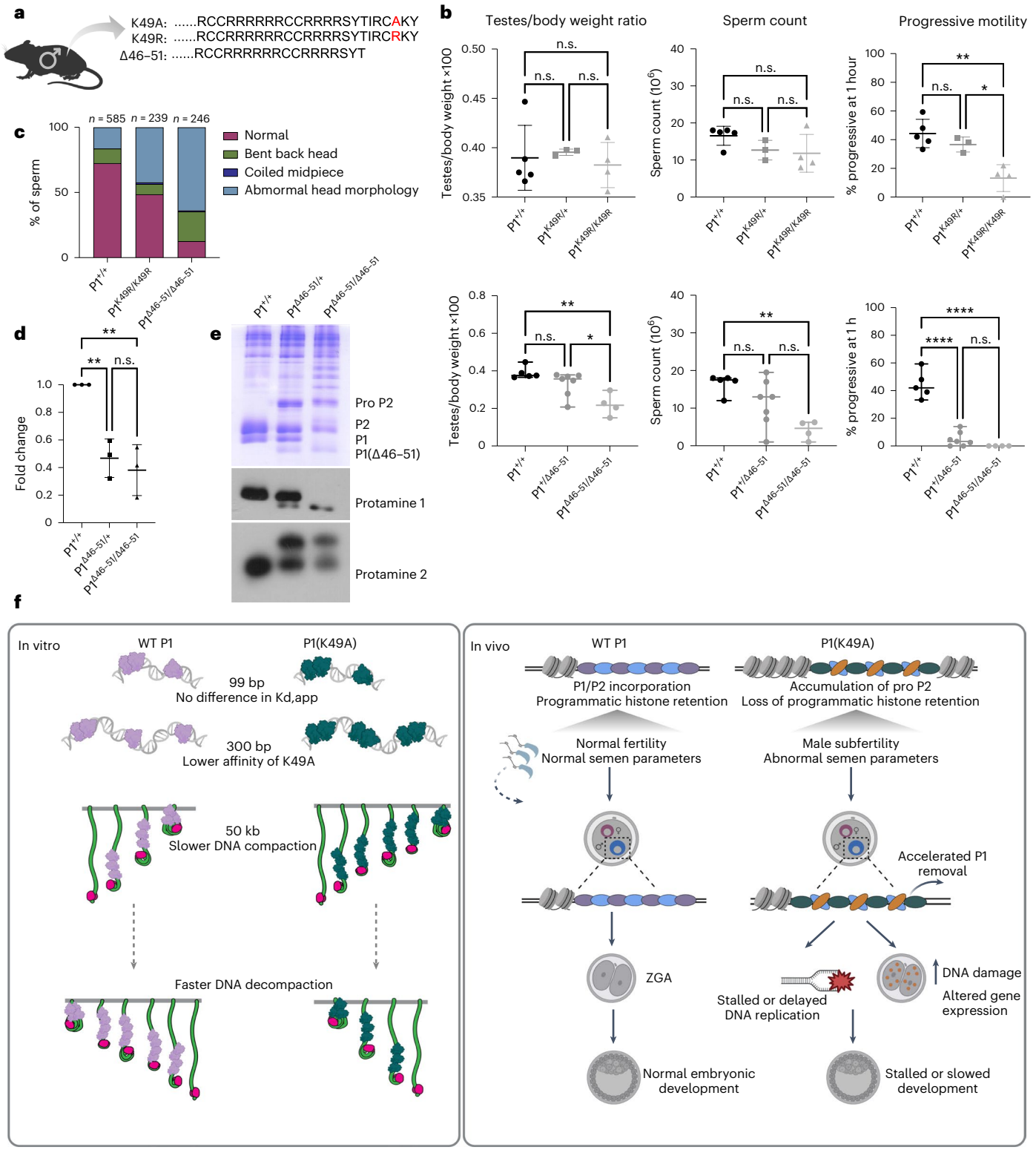

Conservation of the K49 residue across the rodent lineage led us to hypothesize that it evolved to play a species-specific part in spermiogenesis and/or embryonic development. Canonical histone retention and accumulation of pro P2 more than doubled when K49 was substituted with an alanine residue, and in K49A mutant sperm, histone retention became more stochastic genome-wide, shifting from preferential occupancy at promoters to increased occupancy at intronic and intergenic regions. Such increased histone retention may result from the lower affinity of P1(K49A) for DNA, or from disruption of K49ac-mediated recruitment or targeting by remodeling factors to specific genome regions. Previously, it has been shown that both bromodomains of BRDT are needed to induce nucleosome eviction in round spermatids and large-scale acetylation-dependent chromatin reorganization in sperm[47,49,71,72]. Thus, we conceivably hypothesize that BRDT may read and interact with both acetylated histone H4 and acetylated P1 to modulate this process.

Given the defects in histone-to-protamine exchange in P1$^{K49A/K49A}$ sperm, it is not surprising that the mutant sperm have largely lost

Fig. 7 | Defects in P1$^{K49A/K49A}$ males are not driven simply by changes to protamine–DNA electrostatics. a, Cartoon schematic of additional modifications made to mouse P1. **b**, Testes/body weight ratio, total sperm count, and progressive sperm motility for P1(K49R) and P1(Δ46-51) lines. For K49R phenotyping, data were collected from a total of $n = 5$ P1$^{+/+}$ males, $n = 3$ P1$^{K49R/+}$ males, and $n = 4$ P1$^{K49R/K49R}$ males. For P1Δ46–51 phenotyping, data were collected from $n = 5$ P1$^{+/+}$ males, $n = 7$ P1$^{Δ46–51/+}$ males, and $n = 4$ P1$^{Δ46–51/Δ46–51}$ males. Each dot represents a measurement from a single animal. Statistical tests were performed using a one-way ANOVA and were adjusted for multiple comparisons. For P1(Δ46–51) testes to body weight ratio, $P = 0.0014$ between P1$^{+/+}$ and P1$^{Δ46–51/Δ46–51}$, $P = 0.0182$ between P1$^{Δ46–51/+}$ and P1$^{Δ46–51/Δ46–51}$; for P1(Δ46–51) sperm count, $P = 0.0041$ between P1$^{+/+}$ and P1$^{Δ46–51/Δ46–51}$; for P1 Δ46–51 progressive motility, $P = 0.000000453$ between P1$^{+/+}$ and P1$^{Δ46–51/Δ46–51}$ and $P = 0.000000361$ between P1$^{+/+}$ and P1$^{Δ46–51/+}$. For P1(K49R) progressive motility, $P = 0.0014$ between P1$^{+/+}$ and P1$^{K49R/K49R}$, $P = 0.0178$ between P1$^{K49R/+}$ and P1$^{K49R/K49R}$. For all plots, the center line represents the mean and error bars represent the s.d. **c**, Quantification of sperm morphological abnormalities observed in WT, homozygous P1(K49R), and homozygous P1 Δ46–51 males. A total of $n = 585$ WT, $n = 239$ P1$^{K49R/K49R}$, and $n = 246$ P1$^{Δ46–51/Δ46–51}$ sperm were assessed. **d**, Quantification of RNA expression in P1$^{+/+}$, P1$^{Δ46-51/+}$, and P1$^{Δ46-51/Δ46-51}$ testes. Data were collected from $n = 3$ biologically independent samples, and each data point represents measurement from a single biological sample. A total of $n = 3$ technical replicates were performed from each biological sample and averaged for the final value. The center line represents the mean and error bars represent the s.d. Statistical tests were performed using a one-way ANOVA and were adjusted for multiple comparisons, $P = 0.0066$ between P1$^{+/+}$ and P1$^{Δ46-51/+}$, $P = 0.0031$ between P1$^{+/+}$ and P1$^{Δ46-51/Δ46-51}$. **e**, Acid urea gel electrophoresis of sperm basic proteins reveals lower efficiency of incorporation of the truncated P1 protein into sperm chromatin and an alteration in P1:P2 ratio in both P1$^{Δ46-51/+}$ and P1$^{Δ46-51/Δ46-51}$ sperm. Shown is a representative acid urea gel and immunoblot, and similar results were obtained from n = 3 independent males. **f**, Model of in vivo and in vitro consequences of the P1(K49A) substitution.

progressive motility, leading to subfertility. The morphological defects in P1$^{K49A/K49A}$ sperm resemble defects observed in mice that are haploinsufficient for P1, lack P2, or lack TNP1 and TNP2, suggesting that these morphological abnormalities are globally representative of general packaging abnormalities[13,14,18,19]. However, the localization of many abnormalities to the sperm head–neck connection suggests that protamine incorporation is linked to cytoskeleton remodeling or manchette formation in elongating spermatids, consistent with reported interactions between phosphorylated P1 and the inner nuclear membrane lamin-B receptor[73].

Given the large net-positive charge of arginine-rich protamines, their interaction with DNA is undoubtedly electrostatic. However, our data suggest that other determinants also shape protamine–DNA interactions. Wild-type P1 and P1(K49A) have no difference in binding affinity on a 99-bp DNA fragment, but affinity appears to be length-dependent as it differs on 300-bp and 50-kb fragments. In addition, small differences in protamine protein concentration led to unexpectedly large changes in the extent and velocity of compaction in DNA curtain assays, indicating that binding modes are cooperative and likely tightly regulated by local concentrations during in vivo spermiogenesis.

The P1(K49A) protein dissociates from DNA significantly faster than does wild-type P1. Thus, modifications or variations in P1 residues in the C terminus may regulate protamine packaging in sperm and unpackaging following fertilization. Importantly, it seems in mutant embryos, altering the rate or sequence of protamine removal has negative consequences on embryonic development. For example, K49A mutant embryos display delays in DNA replication or temporal uncoupling of DNA replication between maternal and paternal pronuclei. Furthermore, any changes in DNA replication kinetics in mouse and human embryos leads to replication stress, DNA damage, aberrant chromosome segregation, and multipolar spindle division[59,74,75]. Similarly, compared with wild-type, K49A mutant embryos have elevated DNA damage and more micronuclei. Taken together, these data support the likelihood that uncoupling or stalling of replication and increased DNA damage and micronuclei in mutant embryos underlie the significant embryo arrest we observed at the one-cell to two-cell transition and later-stage embryos.

Interfering with DNA replication in mouse and *Xenopus* affects ZGA and gene expression in early embryos[76,77]. Irrespective of DNA replication delays, global ZGA initiates normally in K49A mutant embryos, but genes known to be expressed early in embryos are downregulated, such as cell cycle regulators (*Cdk1*, *Mcm4*, *Incenp*, *Sgo2a*, *Fbxo5*), protein kinases (*Aurka*, *Aurkb*, *Dclk1*, *Pbk*, and *Dyrk44*), chromosome segregation-associated genes (*Zscan*, *Zbtb7c*, *Sgo2a*, *Kntc1*, *Aurka*, and *Aurkb*), and DSB repair-associated genes (*Msh2*, *Ercc4*, *Aunip*, *Exd2*, *Parp9*)[78,79]. Therefore, alterations in DNA replication, failed DNA damage repair, and altered gene expression all underlie the developmental defects in K49A embryos, in support of a mechanistic link between protamine removal from the paternal genome and downstream DNA replication and ZGA.

Together, our results suggest that controlled protamine-driven chromatin remodeling during spermiogenesis is essential for proper sperm compaction. Similarly in the embryo, is it likely that protamine removal must occur sequentially to allow adequate time for both histone deposition and proper re-establishment of the epigenetic landscape. Therefore, remodeling of the paternal genome via protamine-to-histone exchange may function as a molecular clock that coordinates epigenetic re-establishment with the onset of S phase and initiation of DNA replication. Accelerated timing may thus negatively affect replication and gene expression at the two-cell stage, but increased histone retention in mutant sperm may also contribute to alterations observed in mutant embryos. Indeed, mice with abnormal histone retention due to impaired poly ADP-ribose metabolism also displayed altered gene expression in two-cell embryos[80], underscoring the importance of strictly regulating sperm chromatin composition for normal embryonic development.

The P1 K49 residue seems instrumental in protamine biology. How a single amino acid substitution in protamine can cause dramatic alterations when more than 50% of the protein is positively charged is striking. Because substituting K49 for arginine did not rescue spermatogenesis defects, acetylation or the secondary structure conferred by acetylation could have a mechanistic role. Curiously, in both mouse and human protamines, the arginine core is flanked by N- and C-terminal sequences that tend to be highly conserved within, but not across, species. Therefore, it is conceivable that such non-arginine residues evolved to regulate species-specific sperm genome packaging and subsequent unpackaging in the zygote to ensure species compatibility upon fertilization and optimal reproductive fitness.

Online content

Any methods, additional references, Nature Portfolio reporting summaries, source data, extended data, supplementary information, acknowledgements, peer review information; details of author contributions and competing interests; and statements of data and code availability are available at https://doi.org/10.1038/s41594-023-01033-4.

References

1. Tachiwana, H., Osakabe, A., Kimura, H. & Kurumizaka, H. Nucleosome formation with the testis-specific histone H3 variant, H3t, by human nucleosome assembly proteins in vitro. *Nucleic Acids Res.* **36**, 2208–2218 (2008).
2. Tachiwana, H. et al. Structural basis of instability of the nucleosome containing a testis-specific histone variant, human H3T. *Proc. Natl Acad. Sci. USA* **107**, 10454–10459 (2010).
3. Ueda, J. et al. Testis-specific histone variant H3t gene is essential for entry into spermatogenesis. *Cell Rep.* **18**, 593–600 (2017).

4. Barral, S. et al. Histone variant H2A.L.2 guides transition protein-dependent protamine assembly in male germ cells. *Mol. Cell* **66**, 89–101 (2017).
5. Yan, W., Ma, L., Burns, K.H. & Matzuk, M. M. HILS1 is a spermatid-specific linker histone H1-like protein implicated in chromatin remodeling during mammalian spermiogenesis. *Proc. Natl. Acad. Sci. USA* **100**, 10546–10551 (2003).
6. Montellier, E. et al. Chromatin-to-nucleoprotamine transition is controlled by the histone H2B variant TH2B. *Genes Dev.* **27**, 1680–1692 (2013).
7. Shinagawa, T. et al. Disruption of *Th2a* and *Th2b* genes causes defects in spermatogenesis. *Development* **142**, 1287–1292 (2015).
8. Meistrich, M. L., Trostle-Weige, P. K., Lin, R., Bhatnagar, Y. M. & Allis, C. D. Highly acetylated H4 is associated with histone displacement in rat spermatids. *Mol. Reprod. Dev.* **31**, 170–181 (1992).
9. Shirakata, Y., Hiradate, Y., Inoue, H., Sato, E. & Tanemura, K. Histone h4 modification during mouse spermatogenesis. *J. Reprod. Dev.* **60**, 383–387 (2014).
10. Lu, L. Y. et al. RNF8-dependent histone modifications regulate nucleosome removal during spermatogenesis. *Dev. Cell* **18**, 371–384 (2010).
11. Abe, H., Meduri, R., Li, Z., Andreassen, P. R. & Namekawa, S. H. RNF8 is not required for histone-to-protamine exchange in spermiogenesis. *Biol. Reprod.* **105**, 1154–1159 (2021).
12. Sin, H.-S. et al. RNF8 regulates active epigenetic modifications and escape gene activation from inactive sex chromosomes in post-meiotic spermatids. *Genes Dev.* **26**, 2737–2748 (2012).
13. Shirley, C. R., Hayashi, S., Mounsey, S., Yanagimachi, R. & Meistrich, M. L. Abnormalities and reduced reproductive potential of sperm from Tnp1- and Tnp2-null double mutant mice. *Biol. Reprod.* **71**, 1220–1229 (2004).
14. Yu, Y. E. et al. Abnormal spermatogenesis and reduced fertility in transition nuclear protein 1-deficient mice. *Proc. Natl Acad. Sci. USA* **97**, 4683–4688 (2000).
15. Ward, W. S. & Coffey, D. S. DNA packaging and organization in mammalian spermatozoa: comparison with somatic cells. *Biol. Reprod.* **44**, 569–574 (1991).
16. Wykes, S. M. & Krawetz, S. A. The structural organization of sperm chromatin. *J. Biol. Chem.* **278**, 29471–29477 (2003).
17. Cho, C. et al. Haploinsufficiency of protamine-1 or -2 causes infertility in mice. *Nat. Genet.* **28**, 82–86 (2001).
18. Schneider, S. et al. Re-visiting the protamine-2 locus: deletion, but not haploinsufficiency, renders male mice infertile. *Sci. Rep.* **6**, 36764 (2016).
19. Takeda, N. et al. Viable offspring obtained from Prm1-deficient sperm in mice. *Sci. Rep.* **6**, 27409 (2016).
20. Merges, G. E. et al. Loss of Prm1 leads to defective chromatin protamination, impaired PRM2 processing, reduced sperm motility and subfertility in male mice. *Development* **149**, dev200330 (2022).
21. Arévalo, L. et al. Loss of the cleaved-protamine 2 domain leads to incomplete histone-to-protamine exchange and infertility in mice. *PLoS Genet.* **18**, e1010272 (2022).
22. Green, G. R., Balhorn, R., Poccia, D. L. & Hecht, N. B. Synthesis and processing of mammalian protamines and transition proteins. *Mol. Reprod. Dev.* **37**, 255–263 (1994).
23. Yelick, P. C. et al. Mouse protamine 2 is synthesized as a precursor whereas mouse protamine 1 is not. *Mol. Cell. Biol.* **7**, 2173–2179 (1987).
24. Aoki, V. W. et al. Sperm protamine 1/protamine 2 ratios are related to in vitro fertilization pregnancy rates and predictive of fertilization ability. *Fertil. Steril.* **86**, 1408–1415 (2006).
25. de Mateo, S. et al. Protamine 2 precursors (Pre-P2), protamine 1 to protamine 2 ratio (P1/P2), and assisted reproduction outcome. *Fertil. Steril.* **91**, 715–722 (2009).
26. Zatecka, E. et al. The effect of tetrabromobisphenol A on protamine content and DNA integrity in mouse spermatozoa. *Andrology* **2**, 910–917 (2014).
27. Balhorn, R., Brewer, L. & Corzett, M. DNA condensation by protamine and arginine-rich peptides: analysis of toroid stability using single DNA molecules. *Mol. Reprod. Dev.* **56**, 230–234 (2000).
28. Bench, G. S., Friz, A. M., Corzett, M. H., Morse, D. H. & Balhorn, R. DNA and total protamine masses in individual sperm from fertile mammalian subjects. *Cytometry* **23**, 263–271 (1996).
29. Brewer, L. R., Corzett, M. & Balhorn, R. Protamine-induced condensation and decondensation of the same DNA molecule. *Science* **286**, 120–123 (1999).
30. Brewer, L., Corzett, M., Lau, E. Y. & Balhorn, R. Dynamics of protamine 1 binding to single DNA molecules. *J. Biol. Chem.* **278**, 42403–42408 (2003).
31. Prieto, M. C., Maki, A. H. & Balhorn, R. Analysis of DNA–protamine interactions by optical detection of magnetic resonance. *Biochemistry* **36**, 11944–11951 (1997).
32. Krawetz, S. A. & Dixon, G. H. Sequence similarities of the protamine genes: implications for regulation and evolution. *J. Mol. Evol.* **27**, 291–297 (1988).
33. Lewis, J. D., Song, Y., de Jong, M. E., Bagha, S. M. & Ausió, J. A walk though vertebrate and invertebrate protamines. *Chromosoma* **111**, 473–482 (2003).
34. Wyckoff, G. J., Wang, W. & Wu, C.-I. Rapid evolution of male reproductive genes in the descent of man. *Nature* **403**, 304–309 (2000).
35. Queralt, R. et al. Evolution of protamine P1 genes in mammals. *J. Mol. Evol.* **40**, 601–607 (1995).
36. Rooney, A. P., Zhang, J. & Nei, M. An unusual form of purifying selection in a sperm protein. *Mol. Biol. Evol.* **17**, 278–283 (2000).
37. Torgerson, D. G., Kulathinal, R. J. & Singh, R. S. Mammalian sperm proteins are rapidly evolving: evidence of positive selection in functionally diverse genes. *Mol. Biol. Evol.* **19**, 973–980 (2002).
38. Brunner, A. M., Nanni, P. & Mansuy, I. M. Epigenetic marking of sperm by post-translational modification of histones and protamines. *Epigenetics Chromatin* **7**, 2 (2014).
39. Soler-Ventura, A. et al. Characterization of human sperm protamine proteoforms through a combination of top-down and bottom-up mass spectrometry approaches. *J. Proteome Res.* **19**, 221–237 (2020).
40. Chira, F. et al. Phosphorylation of human sperm protamines HP1 and HP2: identification of phosphorylation sites. *Biochim. Biophys. Acta* **1203**, 109–114 (1993).
41. Itoh, K. et al. Dephosphorylation of protamine 2 at serine 56 is crucial for murine sperm maturation in vivo. *Sci. Signal* **12**, eaao7232 (2019).
42. Pirhonen, A., Linnala-Kankkunen, A. & Menpaa, P. H. P2 protamines are phosphorylated in vitro by protein kinase C, whereas P1 protamines prefer cAMP-dependent protein kinase. A comparative study of five mammalian species. *Eur. J. Biochem.* **223**, 165–169 (1994).
43. Seligman, J., Zipser, Y. & Kosower, N. S. Tyrosine phosphorylation, thiol status, and protein tyrosine phosphatase in rat epididymal spermatozoa. *Biol. Reprod.* **71**, 1009–1015 (2004).
44. Gou, L. T. et al. Initiation of parental genome reprogramming in fertilized oocyte by splicing kinase SRPK1-catalyzed protamine phosphorylation. *Cell* **180**, 1212–1227 (2020).
45. Hogarth, C. A. et al. Turning a spermatogenic wave into a tsunami: synchronizing murine spermatogenesis using WIN 18,446. *Biol. Reprod.* **88**, 40 (2013).
46. Griswold, M. & Hogarth, C. Synchronizing spermatogenesis in the mouse. *Biol. Reprod.* **107**, 1159–1165 (2022).
47. Dong, Y. et al. EPC1/TIP60-mediated histone acetylation facilitates spermiogenesis in mice. *Mol. Cell. Biol.* **37**, e00082–17 (2017).

48. Ketchum, C. C., Larsen, C. D., McNeil, A., Meyer-Ficca, M. L. & Meyer, R. G. Early histone H4 acetylation during chromatin remodeling in equine spermatogenesis. *Biol. Reprod.* **98**, 115–129 (2018).
49. Luense, L. J. et al. Gcn5-mediated histone acetylation governs nucleosome dynamics in spermiogenesis. *Dev. Cell* **51**, 745–758 (2019).
50. Shiota, H. et al. Nut directs p300-dependent, genome-wide H4 hyperacetylation in male germ cells. *Cell Rep.* **24**, 3477–3487 (2018).
51. Chereji, R. V., Bryson, T. D. & Henikoff, S. Quantitative MNase-seq accurately maps nucleosome occupancy levels. *Genome Biol.* **20**, 198 (2019).
52. Hammoud, S. S. et al. Distinctive chromatin in human sperm packages genes for embryo development. *Nature* **460**, 473–478 (2009).
53. Hisano, M. et al. Genome-wide chromatin analysis in mature mouse and human spermatozoa. *Nat. Protoc.* **8**, 2449–2470 (2013).
54. Brykczynska, U. et al. Repressive and active histone methylation mark distinct promoters in human and mouse spermatozoa. *Nat. Struct. Mol. Biol.* **17**, 679–687 (2010).
55. Yin, Q. et. al. Revisiting chromatin packaging in mouse sperm. Preprint at *bioRxiv* https://doi.org/10.1101/2022.12.26.521943 (2022).
56. Casadio, F. et al. H3R42me2a is a histone modification with positive transcriptional effects. *Proc. Natl Acad. Sci. USA* **110**, 14894–14899 (2013).
57. Balhorn, R. The protamine family of sperm nuclear proteins. *Genome Biol.* **8**, 227 (2007).
58. Aoki, E. & Schultz, R. M. DNA replication in the 1-cell mouse embryo: stimulatory effect of histone acetylation. *Zygote* **7**, 165–172 (1999).
59. Palmerola, K. L. et al. Replication stress impairs chromosome segregation and preimplantation development in human embryos. *Cell* **185**, 2988–3007 (2022).
60. Bryant, H. E. et al. PARP is activated at stalled forks to mediate Mre11-dependent replication restart and recombination. *EMBO J.* **28**, 2601–2615 (2009).
61. Maya-Mendoza, A. et al. High speed of fork progression induces DNA replication stress and genomic instability. *Nature* **559**, 279–284 (2018).
62. Kai, M., Boddy, M. N., Russell, P. & Wang, T. S.-F. Replication checkpoint kinase Cds1 regulates Mus81 to preserve genome integrity during replication stress. *Genes Dev.* **19**, 919–932 (2005).
63. Brooks, K. E. et al. Molecular contribution to embryonic aneuploidy and karyotypic complexity in initial cleavage divisions of mammalian development. *Development* **149**, dev198341 (2022).
64. Aoki, F., Worrad, D. M. & Schultz, R. M. Regulation of transcriptional activity during the first and second cell cycles in the preimplantation mouse embryo. *Dev. Biol.* **181**, 296–307 (1997).
65. Falco, G. et al. Zscan4: a novel gene expressed exclusively in late 2-cell embryos and embryonic stem cells. *Dev. Biol.* **307**, 539–550 (2007).
66. Grow, E. J. et al. p53 convergently activates Dux/DUX4 in embryonic stem cells and in facioscapulohumeral muscular dystrophy cell models. *Nat. Genet.* **53**, 1207–1220 (2021).
67. Hendrickson, P. G. et al. Conserved roles of mouse DUX and human DUX4 in activating cleavage-stage genes and MERVL/HERVL retrotransposons. *Nat. Genet.* **49**, 925–934 (2017).
68. De Iaco, A. et al. DUX-family transcription factors regulate zygotic genome activation in placental mammals. *Nat. Genet.* **49**, 941–945 (2017).
69. De Iaco, A., Verp, S., Offner, S., Grun, D. & Trono, D. DUX is a non-essential synchronizer of zygotic genome activation. *Development* **147**, dev177725 (2020).
70. Gao, Y. et al. Protein expression landscape of mouse embryos during pre-implantation development. *Cell Rep.* **21**, 3957–3969 (2017).
71. Boussouar, F. et al. A specific CBP/p300-dependent gene expression programme drives the metabolic remodelling in late stages of spermatogenesis. *Andrology* **2**, 351–359 (2014).
72. Gaucher, J. et al. Bromodomain-dependent stage-specific male genome programming by Brdt. *EMBO J.* **31**, 3809–3820 (2012).
73. Mylonis, I. et al. Temporal association of protamine 1 with the inner nuclear membrane protein lamin B receptor during spermiogenesis. *J. Biol. Chem.* **279**, 11626–11631 (2004).
74. Wilhelm, T. et al. Spontaneous slow replication fork progression elicits mitosis alterations in homologous recombination-deficient mammalian cells. *Proc. Natl Acad. Sci. USA* **111**, 763–768 (2014).
75. Nakatani, T. et al. DNA replication fork speed underlies cell fate changes and promotes reprogramming. *Nat. Genet.* **54**, 318–327 (2022).
76. Liu, B. & Grosshans, J. in *Zygotic Genome Activation. Methods in Molecular Biology* Vol. 1605 (ed. Lee, K.) 11–30 (Humana Press, 2017).
77. Blythe, S. A. & Wieschaus, E. F. Zygotic genome activation triggers the DNA replication checkpoint at the midblastula transition. *Cell* **160**, 1169–1181 (2015).
78. Zeng, F., Baldwin, D. A. & Schultz, R. M. Transcript profiling during preimplantation mouse development. *Dev. Biol.* **272**, 483–496 (2004).
79. Xue, Z. et al. Genetic programs in human and mouse early embryos revealed by single-cell RNA sequencing. *Nature* **500**, 593–597 (2013).
80. Ihara, M. et al. Paternal poly (ADP-ribose) metabolism modulates retention of inheritable sperm histones and early embryonic gene expression. *PLoS Genet.* **10**, e1004317 (2014).

Publisher's note Springer Nature remains neutral with regard to jurisdictional claims in published maps and institutional affiliations.

Springer Nature or its licensor (e.g. a society or other partner) holds exclusive rights to this article under a publishing agreement with the author(s) or other rightsholder(s); author self-archiving of the accepted manuscript version of this article is solely governed by the terms of such publishing agreement and applicable law.

© The Author(s), under exclusive licence to Springer Nature America, Inc. 2023

[1]Cellular and Molecular Biology Graduate Program, University of Michigan, Ann Arbor, MI, USA. [2]Department of Human Genetics, University of Michigan, Ann Arbor, MI, USA. [3]Department of Obstetrics and Gynecology, University of Michigan, Ann Arbor, MI, USA. [4]Department of Obstetrics, Gynecology and Reproductive Sciences, Magee Womens Research Institute, University of Pittsburgh School of Medicine, Pittsburgh, PA, USA. [5]Department of Molecular, Cellular and Developmental Biology, University of Michigan, Ann Arbor, MI, USA. [6]Department of Biochemistry and Molecular Biotechnology, University of Massachusetts Medical School, Worcester, MA, USA. [7]Departments of Chemistry, Molecular Biosciences, and the National Resource for Translational and Developmental Proteomics, Northwestern University, Evanston, IL, USA. [8]Department of Biological Chemistry, University of Michigan, Ann Arbor, MI, USA. [9]Department of Computational Medicine and Bioinformatics, University of Michigan, Ann Arbor, MI, USA. [10]Department of Biology, Brandeis University, Waltham, MA, USA. [11]Division of Developmental Biology, Cincinnati Children's Hospital Medical Center, Department of Pediatrics, University of Cincinnati College of Medicine, Cincinnati, OH, USA. [12]Department of Urology, University of Michigan, Ann Arbor, MI, USA. [13]These authors contributed equally: Lindsay Moritz, Samantha B. Schon. [14]These authors jointly supervised this work: Sy Redding, Saher Sue Hammoud. ✉e-mail: hammou@med.umich.edu

Methods

Lead contact and materials availability

Additional information and requests for resources and reagents should be directed to and will be fulfilled by the lead contact, S.S.H. (hammou@med.umich.edu). All unique reagents generated in this study are available from the lead contact with a completed Materials Transfer Agreement.

Mice

Experiments using animals (*Mus musculus)* were carried out with prior approval of the University of Michigan Institutional Committee on Use and Care of Animals (PRO00006047, PRO00008135, PRO00010000) and in accordance with the guidelines established by the National Research Council Guide for the Care and Use of Laboratory Animals. Mice were housed in the University of Michigan animal facility in an environment with controlled light (12 h on/off), temperature (21 to 23 °C), and humidity (30–70%), with ad libitum access to water and food (Lab Diet no. 5008 for breeding mice, no. 5LOD for non-breeding animals).

$P1^{K49A/K49A}$ mice, $P1^{K49R/K49R}$ mice, and $P1^{\Delta 46-51/\Delta 46-51}$ mice were generated on the C57BL/6N background using CRISPR–Cas9-mediated genome editing by the Cincinnati Children's Hospital Transgenic Animal and Genome Editing Core Facility. The single guide RNA (sgRNA) and donor oligonucleotide were designed as previously described[81]. The guide RNA target sequence (5′-GCCGCCGCTCATACACCATAAGG-3′) was selected according to the on- and off-target scores provided by the web tool CRISPOR (v. 5.01)[81] (http://crispor.tefor.net) and proximity to the target site. Ribonucleoprotein (RNP) complexes were formed by mixing sgRNA (80 ng μl^{-1}) with Cas9 protein (IDT, 120 ng μl^{-1}) in Opti-MEM (ThermoFisher) and incubating at 37 °C for 10 min, at which time the donor oligo (IDT, 500 ng μl^{-1}) was added. Zygotes from super-ovulated C57BL/6N females were electroporated with 7 µl of the RNP–donor oligonucleotide mix on ice using a Genome Editor electroporator (BEX; 30 V, 1 ms width, 5 pulses with 1-s intervals). Zygotes were moved to 500 µl cold M2 medium (Sigma), warmed to room temperature, and transferred to oviductal ampullas of pseudopregnant CD-1 females. All animal procedures were carried out in accordance with the Institutional Animal Care and Use Committee and approval of Cincinnati Children's Hospital Medical Center. All mice were backcrossed to the C57BL/6J background, and all mice used for the experiments were male, with the exception of C57BL/6J females used for breeding. Males in all studies were between 8 and 16 weeks of age. Adult (8–16 weeks) females were used solely for breeding.

Antibodies

A rabbit polyclonal antibody against P1(K49ac) was generated at GeneMed Synthesis via immunization of rabbits with the following synthesized peptide: P1 K49ac-CRRRRSYTIRCK(ac)KY. For both immunofluorescence and immunoblotting, the P1(K49ac) antibody was used at a 1:500 dilution. All other antibodies used are specified below, where applicable, and were used at the following dilutions: P1: 1:500, P2: 1:1,000, histone H2B: 1:1,000, histone H3: 1:1,000, histone H4: 1:500, ac-H4: 1:1000, alpha tubulin: 1:1,000, TNP1: 1:100 for immunofluorescence, 1:500 for immunoblotting, TNP2: 1:1,000, V5: 1:1,000, PNA-lectin: 1:1,000, BrdU: 1:500, Zscan4: 1:500, phospho-H2A.X S139: 1:500.

Acid extraction of sperm basic proteins

Sperm pellets were subjected to hypotonic lysis in 1 mM PMSF and spun down at 8,000*g* for 8 min followed by resuspension in 100 µl of 100 mM Tris pH 8.0, 20 mM EDTA, 1 mM PMSF, protein denaturation with 100 µl of 6 M guanidine-HCl, 575 mM DTT, and alkylation with 200 µl of 522 mM sodium iodoacetate for 30 min in the dark. Protein pellets were washed twice with 1 ml cold ethanol and extracted with 800 µl of 0.5 M HCl, 50 mM DTT at 37 °C for 10 min. Supernatants were precipitated overnight at −20 °C with TCA to a final concentration of 20%. The following day, precipitates were spun down at 12,000*g* for 8 min and protein pellets were washed twice in 1 ml of 1% 2-mercaptoethanol in cold acetone. Final protein pellets were resuspended in water[82].

Peptide competition assay to assess antibody specificity

Protamines were first acid-extracted as described above. An increasing amount of protein (0.5 µg and 1 µg for non-specific peptide, 1 µg and 3 µg for non-acetylated P1 peptide) was loaded on each immunoblot. Before adding to immunoblots, antibodies were incubated at room temperature for 30 min, with tenfold excess of specific or non-specific peptide, or alone with no peptide. After blocking, blots were incubated for 1.5 h in either antibody only, antibody with specific peptide, or antibody with non-specific peptide. The non-specific peptide used in these assays was N-DSNKEFGTSNESTE-C and the non-acetylated P1 peptide used was N-CRRRRSYTIRSKKY-C.

Mass spectrometry of mouse protamine PTMs

Mass spectrometry of protamine PTMs in mouse sperm was performed at MS BioWorks. Briefly, protamines were first acid-extracted as described above. Then, 20 µg of protein was run in triplicate on a 4–20% SDS–PAGE gel (BioRad), and a single band corresponding to P1 and P2 was cut out for processing. Gel bands were washed with 25 mM ammonium bicarbonate followed by three washes in 100% acetonitrile. Bands were reduced with 10 mM dithiothreitol at 60 °C, followed by alkylation with 50 mM light iodoacetamide at room temperature. Bands were digested with either trypsin (Promega) at 37 °C for 4 h, chymotrypsin (Promega) at 37 °C for 12 h, or lys-C (Promega) at 37 °C for 12 h. For all enzymes, digests were quenched with formic acid and supernatants were analyzed. Digests were analyzed by nano LC–MS/MS with a Waters NanoAcquity HPLC system interfaced to a ThermoFisher Q Exactive. Peptides were loaded on a trapping column and eluted over a 75-µm analytical column at 350 nl min^{-1}. Both columns were packed with Luna C18 resin (Phenomenex). The mass spectrometer was operated in data-dependent mode, with MS and MS/MS (15 most abundance ions) performed in the Orbitrap at 70,000 FWHM and 17,500 FWHM resolution, respectively. Data were searched using a local copy of Byonic with the following parameters: enzyme: semi-trypsin or none (for chymotrypsin and lys-C), database: Swissprot Mouse (forward and reverse appended with common), fixed modification: carbamidomethyl (C), variable modifications: oxidation (O), acetyl (protein N-term), deamidation (NQ), phospho (STY), methyl (KR), dimethyl (KR), trimethyl (K), mass values: monoisotopic, peptide mass tolerance (10 ppm), fragment mass tolerance (0.02 Da), max missed cleavages: 2. Mascot DAT files were parsed into the Scaffold software for validation and filtering and to create a non-redundant list per sample. Data were filtered using a minimum protein value of 95% and a minimum peptide value of 50% (Prophet scores), and at least two unique peptides per protein were required. Site localization probabilities were assigned using A-Score[83].

Evolutionary analysis of P1 sequence conservation

The phylogenetic tree was constructed using maximum likelihood (PhyML) inferred from P1 protein sequences for species across the orders Rodentia, Primate, and Artiodactyla using the Whelan and Goldman matrix (WAG) substitution strategy. Sequences were downloaded from NCBI and aligned using standard parameters of MUSCLE[84]. Bootstrap support with 1,000 replicates is shown for each node, with values > 95 indicating strong support.

Immunofluorescence and quantification of seminiferous tubule staging

Adult testes were fixed overnight in 4% PFA at 4 °C before submerging in ethanol and processing for formalin fixed paraffin embedding (FFPE). Five-micrometer-thick tissue sections were deparaffinized followed by

permeabilization and subsequent antigen retrieval via boiling in 10 mM sodium citrate pH 6.0 for 10 min. Following blocking in 1× PBS, 3% BSA, and 500 mM glycine, sections were incubated with primary antibodies overnight at 4 °C. PNA-lectin (GeneTex) was used to stain acrosomes and DAPI was used as a nuclear counterstain. All secondary antibodies (Life Technologies/Molecular Probes) were used at 1:1,000. For assessment of staging, seminiferous tubules were split into categories (I–III, IV–VI, VII–VIII, IX, X–XI, XII) according to their lectin staining pattern and cell types present, as previously described[85].

Synchronization of spermatogenesis in juvenile male mice

Males were pipette-fed the retinoic acid inhibitor WIN 18,446 (100 µg g^{-1} body weight, resuspended in 1% gum tragacanth) daily, beginning when they were 2 days old (2 days post-partum), for 7 days to block spermatogonia differentiation. At 9 days post-partum, males were injected with 100 µg of retinoic acid (in 10 µl DMSO) to synchronously initiate spermatogonia differentiation[46]. Testes were then collected at 23 and 24 days after retinoic acid injection and successful synchronization was confirmed by immunofluorescence (both DAPI staining to assess cell morphology and PNA-lectin).

Subcellular and high-salt chromatin fractionation of synchronized testes

Testes were synchronized as described above and collected at either 23 or 24 days after retinoic acid injection (enriching for stage VIII–X spermatids). Spermatids were fractionated using a high-salt gradient[86]. Briefly, frozen testes were homogenized using a Dounce homogenizer and cells were washed with PBS. Spermatid tails were removed via incubation with 0.1% CTAB for 5 min on ice and cells were then washed several times in 50 mM Tris-HCl pH 8.0. Cells were lysed for 15 min on ice and then centrifuged at 800*g* for 15 min. The supernatant was collected as the cytoplasmic fraction, and the nuclei were subsequently digested with 1 U of MNase at 37 °C for 30 min then quenched with EGTA. Samples were then centrifuged at 400*g* for 10 min, and the supernatant was kept as the MNase fraction. Chromatin was then fractionated by sequential incubations with 0.5 M, 1 M, and 2 M NaCl for 30 min each. Proteins were precipitated from salt fractions using 20% TCA overnight at −20 °C and resuspended in water before immunoblotting.

Phenotypic assessment of $P1^{+/+}$, $P1^{K49A/+}$, and $P1^{K49A/K49A}$ males

All phenotyping was carried out in males between 9 and 12 weeks of age. Sperm were counted using a Makler chamber and performed as $n = 3$ independent technical replicates per mouse. For progressive sperm motility assessment, a minimum of 100 sperm were counted. For quantification of fecundity, 8-week-old males ($n = 3$ per genotype) were individually housed for 3 days before 8-week-old C57BL/6J females were added. Females ($n = 3$ females per male) were checked daily for the presence of copulatory plugs, and once plugs were noted, females were removed and placed in a new cage. The percentage of females that were successfully impregnated was recorded.

Bottom-up MS of mature sperm histone PTMs

Sperm were first pooled from five adult males per genotype. Sperm pellets containing 20 million sperm each were then washed twice with 1 mM PMSF (in water), spun down at 8,000*g* for 8 min, then resuspended in DTT buffer (50 mM DTT with 1 mM PMSF in PBS-100 µl per 10 million sperm) and incubated on ice for 30 min. Sperm were then spun down at 2,500*g* for 5 min and resuspended in hypotonic lysis buffer (10 mM Tris-HCl pH 8.0, 1 mM KCl, 1.5 mM $MgCl_2$, 1 mM DTT) with 1× protease inhibitor and incubated (with rotation) for 20 min at 4 °C. Nuclei were pelleted at 10,000*g* for 10 min before being resuspended in 400 µl of 0.4 N H_2SO_4 and incubated (with rotation) overnight at 4 °C. The following day, samples were spun down at 16,000*g* for 5 min, and the supernatants were transferred to new tubes, followed by the addition of TCA to a final concentration of 20%. Samples were incubated for 6 h at −20 °C. Precipitated protein was then pooled from all samples from a single genotype and pelleted at 12,000*g* for 10 min. Pellets were washed twice with cold 100% acetone prior to being frozen in liquid nitrogen before MS analysis[49]. For MS analysis, each sample was derivatized via propionylation and digested with trypsin, as previously described[87]. Following digestion, each sample was resuspended in 30 µl of 0.1% TFA/mH_2O, and 2 µl was injected; there were three technical replicates per sample.

Bottom-up MS analysis of quantitative histone retention

Histones were first extracted using sulfuric acid as described above. A small aliquot (10%) was removed from each sample during the second acetone wash to determine the amount of input protein per sample. For MS analysis, histones were derivatized using propionic anhydride reagent for 1 h before and following digestion. Histones were then digested with 1 µg of Promega sequencing grade Trypsin overnight at 37 °C. Digests were derivatized with propionic anhydride[88]. Peptide samples were dried in a SpeedVac and resuspended in 0.1% TFA for analysis. Targeted LC–MS/MS was performed on a Thermo TSQ Altis (Thermo Scientific), and raw data were analyzed in Skyline[89], according to published methods[90]. Peptides were analyzed by SRM-LC–MS/MS on three technical replicates per sample, with blanks every three replicates. Raw data were analyzed in Skyline, according to published methods[89,90].

Acid urea gel electrophoresis for the separation of sperm basic proteins

Protamines were first acid-extracted from a fixed number of sperm cells per genotype as described above, with slight modification[91]. Following hypotonic lysis, sperm pellets were incubated in 1 ml of 6 M guanidine-HCl, 500 mM Hepes pH 7.5, and 10 mM DTT for 1 h at room temperature. Cysteine residues were alkylated using vinylpyridine to a final concentration of 250 mM and incubated for 1.5 h at room temperature. Proteins were extracted with 0.9 M HCl and dialyzed overnight at 4 °C against 0.2 M HCl. The following day, insoluble proteins were removed by centrifugation at 12,000*g* for 5 min. Soluble proteins were precipitated with TCA to a final concentration of 20% for 4 h at −20 °C. Precipitated proteins were washed twice with acetone before being resuspended in 0.9 M acetic acid, 8 M urea, and 100 mM β-mercaptoethanol. Acid urea gels were prepared as previously described[92]. P1:P2 ratios were calculated using ImageJ.

Sperm protein extraction for the assessment of histone retention

Sperm pellets containing 5 million–15 million sperm were resuspended in lysis buffer (20 mM Tris pH 7.5, 1 mM $MgCl_2$, 1 mM $CaCl_2$, 137 mM NaCl, 10% glycerol, 1% NP-40, 12.5 U ml^{-1} benzonase, 1× protease inhibitors), sonicated briefly, and rotated for 1 h at 4 °C[49]. For immunoblotting, lanes were loaded by the input number of sperm cells. Owing to variability between antibodies, the following numbers of sperm were loaded for each corresponding antibody: histone H3, histone H2B: 25,000, 50,000, 100,000; histone H4: 100,000, 250,000, 400,000. Each blot was probed for α-tubulin as a loading control to ensure comparative loading.

MNase-Seq of mature mouse sperm

MNase-Seq was performed using several modifications from previous protocols[53,55,93]. First, 30 million sperm per genotype were treated with 5 µl of 20 mg ml^{-1} DNaseI for 15 min at 37 °C. Sperm pellets were washed several times in PBS and treated with 0.5% Triton X-100 and 0.05% L-alpha-phosphatidylcholine for 15 min on ice. Pellets were then centrifuged at 2,500*g* for 5 min, and chromatin was decondensed using 50 mM DTT for 1 h at room temperature. DTT was quenched for 30 min at room temperature with 100 mM *N*-ethylmaleimide. Sperm cells were then lysed in buffer containing 0.25% NP-40 and 0.25% DOC for 30 min

at room temperature prior to the addition of 5 U MNase. Samples were digested at 37 °C for 5 min and centrifuged at 20,000*g* for 20 min and soluble chromatin was collected. Insoluble chromatin was digested a second time with 15 U of MNase at 37 °C for 5 min. Samples were run on a 2% agarose gel and bands corresponding to mononucleosomes were cut out and purified using a Zymo gel extraction kit for sequencing.

MNase-seq data analysis

MNase-seq raw data were first trimmed using cta (v. 0.1.2; https://github.com/ParkerLab/cta) to remove adapters. Reads were aligned to the mouse genome assembly mm10 using bwa mem (v. 0.7.15; -I 200,200,5000 -M)[94]. Duplicates were removed using Picard MarkDuplicates (v. 2.18.27; http://broadinstitute.github.io/picard) and samtools (v.1.7) was used to filter for properly paired and mapped reads pairs with mapping quality ≥30 (ref. 95). Peaks were called using MACS2 callpeak (v. 2.1.1.20160309; options:--SPMR -nomodel–broad–shift -100–extsize 200–keep-dup all)[96]. Peaks were filtered against ENCODE blacklists using bedtools intersect (option -v; v. 2.27.1)[97]. Final peaks were called and filtered using a FDR cut-off of >5%. Metagene plots and heatmaps were made using deeptools (v 3.5.1) computematrix, plotProfile, and plotHeatmap function. A Venn digram was generated using R package VennDiagram (v 1.7.3). For analysis of AT versus GC peak enrichment, peaks were fractionated into shared and disjoint sets (WT only and K49A only) using bedtools intersect[98]. Peaks were required to have 80% mutual overlap between WT and K49A for inclusion in the 'shared' fraction. Conversely, only peaks with no overlap between WT and K49A were included in either disjointed set. In total, 11,385 peaks of the original 12,013 passed this filtering procedure, yielding 189 shared, 10,906 WT-only, and 290 K49A-only peaks. Peaks were annotated with their GC and AT content using bedtools nuc[98]. These data were loaded into an R dataframe and summarized into density plots with ggplot2[99].

Protamine purification and in vitro electrophoretic mobility-shift assays

Following acid extraction of basic proteins from mature sperm (described above), precipitated protein pellets were resuspended in 50 µl of water and brought up to 500 µl in gel filtration buffer (25 mM Hepes pH 7.5, 150 mM NaCl, 5 mM TCEP (TCEP was not pH neutralized)). The solution was then subjected to size-exclusion chromatography using a Superdex S75 column. Peak fractions were identified by absorbance at 214 nm and confirmed by immunoblotting. For in vitro electrophoretic mobility-shift assays, varying concentrations of purified protamines were incubated with 40 nM DNA (280 bp) after the proteins were incubated at 37 °C for 10 min in reaction buffer. DNA was prepared by PCR amplification of mouse genomic DNA using the primers specified in Supplementary Table 8. After 1 h of incubation, EMSA reactions were run on a non-denaturing 0.5× TBE 6% polyacrylamide gel and stained with ethidium bromide (Sigma). Band intensities were quantified using ImageJ.

DNA curtains

Microfluidic devices were constructed and DNA curtain assays were performed as previously described[100,101]. Briefly, a lipid bilayer was coated on the surface of the sample chamber and biotinylated phage DNA was anchored to biotinylated lipids within the bilayer via streptavidin. DNA was then aligned at microfabricated barriers using buffer flow. In all experiments, care was taken to ensure that DNA molecules were separated by at least 2 µm to prevent protamine interactions across DNA molecules.

DNA labeling with Cas9

Recombinant dCas9 protein (IDT Alt-R S.p. dCas9 protein V3) was loaded with a dual guide RNA according to IDT's 'Alt-R CRISPR–Cas9 system – in vitro cleavage of target DNA with RNP complex' protocol, with slight modifications for DNA curtains. dCas9 protein was diluted to 200 nM and incubated with gRNA targeting position 47,752 (5′-AUCUGCUGAUGAUCCCUCCG-3′) at a 1:10 ratio in imaging buffer (1 mg ml^{-1} BSA, 40 mM Tris-HCl, pH 7.5, 50 mM NaCl, 5 mM MgCl2, and 1 mM DTT) and incubated on ice for at least 15 min. Anti-HisAlexa555 (Invitrogen) was added to the reaction at a 1:2 ratio to dCas9 and incubated in the dark for 15 min at room temperature. The fluorescent RNP complex was then diluted to 4 nM in imaging buffer and incubated in the flow cell with DNA for 10 min. Finally, to remove nonspecifically bound proteins, the flow cell was washed with 500 µl of imaging buffer containing 100 µg ml^{-1} heparin.

DNA compaction and decompaction experiments

DNA was maintained in flow at a rate of 0.6 ml min^{-1} (average extension to 90% of contour length) for the duration of compaction and decompaction experiments. Prior to introduction into the flowcell, protamines were incubated at 37 °C for 15 min in imaging buffer. Then, protamine was injected into the flowcell, images were collected at 10 Hz, and compaction was monitored by tracking the motion of dCas9 molecules. Immediately following compaction, collection was shifted to 0.2 Hz and decompaction was monitored by tracking the position of dCas9 molecules.

Intracytoplasmic sperm injections and embryo immunofluorescence

Eight-week-old female B6D2F1/J mice were superovulated via injection of 100 µl of pregnant mare serum gonadotropin (PMSG, Prospec Protein Specialists) ~62 h before oocyte collection, which was followed by injection of 100 µl of human chorionic gonadotropin (hCG, Sigma) ~14 h before oocyte collection. Oocyte collection, sperm collection, and piezo-actuated intracytoplasmic sperm injections were performed as previously described[102]. Embryos were cultured in KSOM (Millipore-Sigma) prior to immunofluorescence analysis.

For embryo immunofluorescence, embryos were collected at the indicated time points after washing in KSOM, treated briefly (30 s–1 min) with Acidic Tyrodes solution (EMD Millipore) to remove the zona pellucida, and fixed in 4% PFA for 10 min. Embryos were permeabilized overnight at 4 °C in PBS with 0.1% Triton X-100 and 3% BSA. The next morning, embryos were permeabilized for 1 h in PBS with 0.5% Triton X-100 and 3% BSA. Embryos were then blocked in PBS with 0.1% Triton X-100, 3% BSA, and 10% fetal bovine serum for 1 h and stained with primary antibodies overnight in blocking buffer (PBS with 0.1% Triton X-100, 3% BSA, and 10% fetal bovine serum) at 4 °C. The following day, embryos were washed in PBS with 0.1% Triton X-100 and 3% BSA 5 times for 15 min each, followed by incubation in secondary antibodies (Life Technologies/Molecular Probes) and DAPI (Sigma) for 2 h at room temperature. All images were taken on a Nikon A1R-HD25 confocal microscope (multiple Z plane images were taken for each embryo) and processed with ImageJ.

For BrdU incorporation, embryos were incubated in 10 µM BrdU for 1 h beginning at 7 hpf and collected at 8 hpf. After 1 h of permeabilization in PBS with 0.5% Triton X-100 and 3% BSA, embryos were washed twice in PBS with 0.05% Tween-20 for 10 min. DNA was denatured in 4 N HCl at 37 °C for 10 min, followed by neutralization in 100 mM Tris-HCl pH 8.5 for 30 min at room temperature. Embryos were washed in PBS with 0.05% Tween-20 before blocking in PBS with 0.1% Triton X-100, 3% BSA, and 10% fetal bovine serum for 1 h at room temperature. Embryos were stained with an anti-BrdU antibody (Abcam ab6326, 1:250) overnight at 4 °C.

Single embryo RNA-seq experiments

Two-cell embryos were collected between 26 and 28 hpf. Each embryo was placed into a single well of a plexWell Rapid Single Cell plate (SmartSeq Platform), which was frozen until all embryos were collected and ready for processing. Single cells in lysis reagent were subjected to library prep with PlexWell scRNA reagents (seqWell), following the

manufacturer's protocol. Briefly, each two-cell embryo was lysed and underwent cDNA synthesis and amplification including the addition of unique barcoded adapters. Barcoded cDNAs were pooled before the final PCR amplification. Final library quality was assessed using the LabChip GX (PerkinElmer). Pooled libraries were subjected to 150-bp paired-end sequencing on the NovaSeq6000 (Illumina platform). Bcl2fastq2 Conversion Software (Illumina) was used to generate demultiplexed Fastq files. Sequencing reads were trimmed using Cutadapt v2.3 (ref. 103). FastQC v0.11.8 was used to ensure data quality, and Fastq Screen v was used to screen for contamination[104,105]. Reads were mapped to the reference genome GRCm38 using STAR v2.7.8a[106] and assigned count estimates to genes with RSEM v1.3.3 (ref. 107). Alignment options followed ENCODE standards for RNA-seq. Data from both WT and mutant embryos were compared with previously published data across multiple embryonic stages (GSE45719)[75,108].

Our raw RNA-seq data contained 48 two-cell embryo samples and 32,403 genes (GSE225271). We retained 27 samples that passed a library size filter (total read count >100,000), and normalized read counts to counts per million (CPM). We then selected 14,750 genes with 0 counts in fewer than half of the sample. This data matrix was $\log_{(2)}$-converted, after a floor of 0.5 was added to all the CPM values. Only 12,478 of the 14,750 genes had gene symbols, of which 9,690 can be matched to the gene symbols in the data downloaded from GSE45719 (see below). The analysis shown in Fig. 6e focused on the 27 two-cell samples.

The reference data downloaded from GSE45719 contained 22,431 genes and 317 samples, of which we selected the 286 samples corresponding to ten annotated sample groups: Zygote, Early2, Mid2, Late2, 4Cell, 8Cell, 16Cell, Earlyblast, Midblast, and Lateblast. We selected 12,034 genes with fewer than 250 zero counts among the 317 samples, normalized read counts to CPM, and log-transformed them with a floor of 0.5.

To calculate the cross-correlation matrix between the 27 samples in our data and the 286 samples in GSE45719, we used the 9,690 genes that overlapped between the two datasets, and further selected the highly expressed genes in both datasets with a moderate cut-off, which slightly reduced 9,690 genes to 7,895. The 27-by-286 correlation coefficient matrix was obtained using the logged data, and shown in Fig. 6e, with color range: blue-minimal value of 0.141; red-maximal value of 0.701.

Statistics and reproducibility

All statistical analyses were performed using the GraphPad Prism software. Statistical details, including the exact statistical test used, exact *n* value, what *n* represents, dispersion measures, and significance values are presented in each corresponding figure legend. Where applicable, the reproducibility (that is, the number of replicates and/or number of independent experiments performed with similar results) of the experiment is stated in the corresponding legend. Existing literature informed general sample size, but no statistical method was used to predetermine the sample sizes. No data were excluded from analyses, aside from a select number of embryos for single-embryo RNA-seq that did not meet quality-control thresholds or that had not progressed to the two-cell stage at time of collection. Experiments involving comparison between genotypes (that is, WT versus K49A) were randomized, and investigators were blinded to the genotype.

Reporting summary

Further information on research design is available in the Nature Portfolio Reporting Summary linked to this article.

Data availability

Relevant raw data are supplied in the source data file. All DNA tracking data are available at https://github.com/ReddingLab/Moritz_et_al_2021. Raw video files are available upon request. The MS proteomics data were searched against the Swissprot Mouse database and have been deposited to the ProteomeXchange Consortium via the PRIDE partner repository[109] with the dataset identifier PXD028917 for protamine PTM analysis and via MassIVE with the dataset identifier MSV000091920. All raw and processed genomic data files for single embryo sequencing and MNase-seq experiments are available under the GEO accession number GSE225271. Single-embryo RNA-seq samples were compared with previously published data across multiple embryonic stages (GSE45719). Source data are provided with this paper.

Code availability

DNA tracking code is available at https://github.com/ReddingLab/Moritz_et_al_2021.

References

81. Haeussler, M. et al. Evaluation of off-target and on-target scoring algorithms and integration into the guide RNA selection tool CRISPOR. *Genome Biol.* **17**, 148 (2016).
82. Liu, L., Aston, K. I. & Carrell, D. T. Protamine extraction and analysis of human sperm protamine 1/protamine 2 ratio using acid gel electrophoresis. *Methods Mol. Biol.* **927**, 445–450 (2013).
83. Beausoleil, S. A., Villen, J., Gerber, S. A., Rush, J. & Gygi, S. P. A probability-based approach for high-throughput protein phosphorylation analysis and site localization. *Nat. Biotechnol.* **24**, 1285–1292 (2006).
84. Edgar, R. C. MUSCLE: a multiple sequence alignment method with reduced time and space complexity. *BMC Bioinformatics* **5**, 113 (2004).
85. Nakata, H., Wakayama, T., Takai, Y. & Iseki, S. Quantitative analysis of the cellular composition in seminiferous tubules in normal and genetically modified infertile mice. *J. Histochem. Cytochem.* **63**, 99–113 (2015).
86. Herrmann, C., Avgousti, D. & Weitzman, M. Differential salt fractionation of nuclei to analyze chromatin-associated proteins from cultured mammalian cells. *Bio. Protoc.* **7**, e2175 (2017).
87. Garcia, B. A., Shabanowitz, J. & Hunt, D. F. Characterization of histones and their post-translational modifications by mass spectrometry. *Curr. Opin. Chem. Biol.* **11**, 66–73 (2007).
88. Garcia, B. A. et al. Chemical derivatization of histones for facilitated analysis by mass spectrometry. *Nat. Protoc.* **2**, 933–938 (2007).
89. MacLean, B. et al. Skyline: an open source document editor for creating and analyzing targeted proteomics experiments. *Bioinformatics* **26**, 966–968 (2010).
90. Camarillo, J. M. et al. Coupling fluorescence-activated cell sorting and targeted analysis of histone modification profiles in primary human leukocytes. *J. Am. Soc. Mass. Spectrom.* **30**, 2526–2534 (2019).
91. Giorgini, F., Davies, H. G. & Braun, R. E. Translational repression by MSY4 inhibits spermatid differentiation in mice. *Development* **129**, 3669–3679 (2002).
92. de Yebra, L. & Oliva, R. Rapid analysis of mammalian sperm nuclear proteins. *Anal. Biochem.* **209**, 201–203 (1993).
93. Erkek, S. et al. Molecular determinants of nucleosome retention at CpG-rich sequences in mouse spermatozoa. *Nat. Struct. Mol. Biol.* **20**, 868–875 (2013).
94. Li, H. & Durbin, R. Fast and accurate short read alignment with Burrows–Wheeler transform. *Bioinformatics* **25**, 1754–1760 (2009).
95. Li, H. et al. The Sequence Alignment/Map format and SAMtools. *Bioinformatics* **25**, 2078–2079 (2009).
96. Zhang, Y. et al. Model-based Analysis of ChIP–seq (MACS). *Genome Biol.* **9**, R137 (2008).
97. Quinlan, A. R. BEDTools: The Swiss-Army Tool for Genome Feature Analysis. *Curr. Protoc. Bioinformatics* **47**, 11.12.1-34 (2014).
98. Quinlan, A. R. & Hall, I. M. BEDTools: a flexible suite of utilities for comparing genomic features. *Bioinformatics* **26**, 841–842 (2010).

99. Wickham, H. *ggplot2* (Springer Cham, 2016).
100. Gallardo, I. F. et al. High-throughput universal DNA curtain arrays for single-molecule fluorescence imaging. *Langmuir* **31**, 10310–10317 (2015).
101. Larson, A. G. et al. Liquid droplet formation by HP1α suggests a role for phase separation in heterochromatin. *Nature* **547**, 236–240 (2017).
102. Yoshida, N. & Perry, A. C. Piezo-actuated mouse intracytoplasmic sperm injection (ICSI). *Nat. Protoc.* **2**, 296–304 (2007).
103. Martin, M. Cutadapt removes adapter sequences from high-throughput sequencing reads. *EMBnet. J.* **17**, 10 (2011).
104. Andrews, S. FastQC: A quality control tool for high throughput sequence data. (2010).
105. Wingett, S. W. & Andrews, S. FastQ Screen: a tool for multi-genome mapping and quality control. *F1000Res.* **7**, 1338 (2018).
106. Dobin, A. et al. STAR: ultrafast universal RNA-seq aligner. *Bioinformatics* **29**, 15–21 (2013).
107. Li, B. & Dewey, C. N. RSEM: accurate transcript quantification from RNA-Seq data with or without a reference genome. *BMC Bioinf.* **12**, 323 (2011).
108. Deng, Q., Ramsköld, D., Reinius, B. & Sandberg, R. Single-cell RNA-seq reveals dynamic, random monoallelic gene expression in mammalian cells. *Science* **343**, 193–196 (2014).
109. Perez-Riverol, Y. et al. The PRIDE database and related tools and resources in 2019: improving support for quantification data. *Nucleic Acids Res.* **47**, D442–D450 (2019).

Acknowledgements

We thank members of the Hammoud lab for scientific discussions and comments on the manuscript; Y.-C. Hu and members of the Cincinnati Children's Hospital Transgenic Animal and Genome Editing Core Facility; T. Saunders and members of the University of Michigan Transgenic Animal Model Core; members of the Bardwell lab for assistance with fluorescence anisotropy; H. Malik, R. Schultz, and A. Peters for scientific and experimental discussion; and H. Schorle for providing essential reagents and for scientific and experimental discussion. Portions of Figs. 2, 4, and 7 were created with BioRender.com. This research was supported by National Institute of Health (NIH) grants 1R21HD090371-01A1 (S.S.H.), 1DP2HD091949-01 (S.S.H.), R01 HD104680 01 (S.S.H.), 1R35GM147477-01 (S.R.), UCSF Program for Breakthrough Biomedical Research provided by the Sandler Foundation (S.R.), 5K12 HD065257-07 (S.B.S.), 1R03HD10150101A1 (S.B.S.), R01-AG050509 (J.N.), R01-GM120094 (J.N.), R35GM137832 (K.R.), training grants NSF 1256260 DGE (L.M.), Rackham Predoctoral Fellowship (L.M.), T32GM007315 (L.M.), an American Cancer Society Research Scholar grant RSG-17-037-01-DMC (J.N.), an American Heart Association predoctoral fellowship award ID: 830111 (R.A.), and Open Philanthropy Grant 2019-199327 (5384) (S.S.H.).

Author contributions

S.S.H., L.M., and S.B.S. contributed to overall project design. L.M., S.B.S., M.R., J.G.-K., C.S., and J.C. performed experiments. Y.S. performed ICSI experiments. R.A. assisted with purification of protamines using chromatography for in vitro biochemistry. J.M.C. performed MS experiments with N.L.K.'s oversight. M.R.B. performed analysis of fluorescence anisotropy data with oversight from P.J.O. A.G.D. and A.P.B. aided in MNase-seq analysis of sperm. S.R. performed DNA curtain experiments. Y.-C.H. generated P1(K49A) mice. J.Z.L. analyzed single embryo RNA-seq data. General project insight was provided by K.R., J.N., J.Z.L., K.E.O., S.R., and S.S.H. L.M. and S.S.H. wrote the manuscript, with input from S.R. All authors provided comments on the manuscript.

Competing interests

The authors have no competing interests.

Additional information

Extended data is available for this paper at https://doi.org/10.1038/s41594-023-01033-4.

Supplementary information The online version contains supplementary material available at https://doi.org/10.1038/s41594-023-01033-4.

Correspondence and requests for materials should be addressed to Saher Sue Hammoud.

Peer review information : *Nature Structural & Molecular Biology* thanks Arne Gennerich, Clinton Lau and the other, anonymous, reviewer(s) for their contribution to the peer review of this work. Carolina Perdigoto and Dimitris Typas were the primary editors on this article and managed its editorial process and peer review in collaboration with the rest of the editorial team.

Reprints and permissions information is available at www.nature.com/reprints.

https://doi.org/10.1038/s41594-023-01033-4

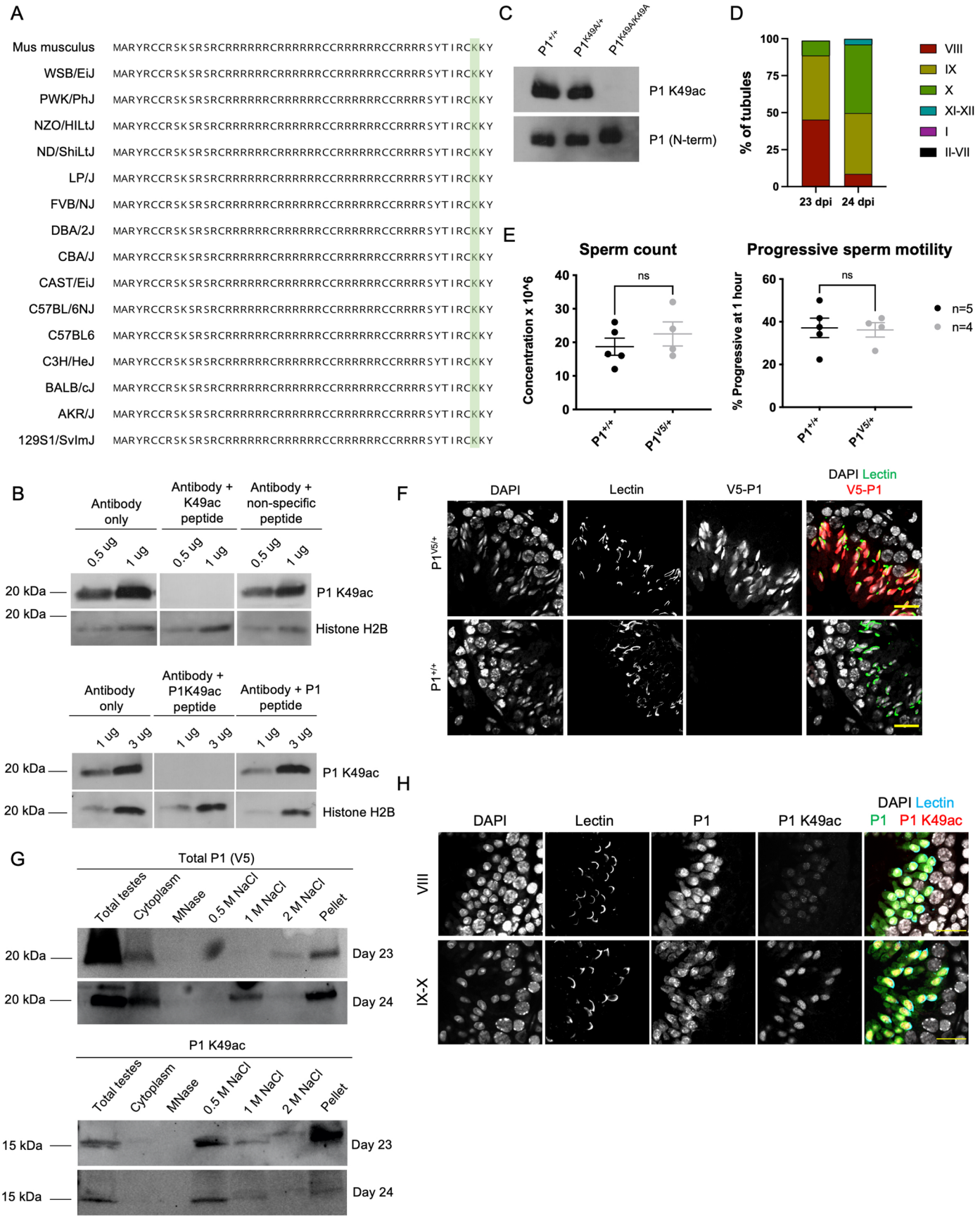

Extended Data Fig. 1 | See next page for caption.

https://doi.org/10.1038/s41594-023-01033-4

Extended Data Fig. 1 | The P1 K49 residue is highly conserved across the mouse lineage and the custom antibody against P1 K49ac is specific. (**a**) Alignment of P1 amino acid sequences across multiple mouse species illustrates conservation of P1. (**b**) Immunoblot of acid extracted protein lysates from mature sperm illustrates a clear band for P1 K49ac that is competed off only in the presence of a specific peptide containing acetylated P1 at K49 (top blot using a non-specific, unrelated peptide and bottom blot using a P1 non-acetylated peptide). Shown are representative immunoblots and similar results were obtained from n = 3 independent experiments. (**c**) Acid urea immunoblot of protein lysates from $P1^{+/+}$, $P1^{K49A/+}$, and $P1^{K49A/K49A}$ sperm probed for P1 K49ac illustrates specificity of the antibody. Shown is a representative blot and similar results were obtained from n = 2 experiments. (**d**) Quantification of synchronization efficiency in testes collected 23- and 24 days-post retinoic acid (RA) injection illustrates successful synchronization and enrichment of stage VIII-X elongating spermatids. Similar results were obtained from n = 4 independent experiments. (**e**) Total epididymal sperm count (left) and progressive sperm motility after 1 hour (right) for $P1^{+/+}$ and $P1^{V5/+}$ males (n = 5 $P1^{+/+}$ males and n = 4 $P1^{V5/+}$ males). Statistical test was performed using an unpaired, two-tailed t-test, p = 0.4032 for sperm count and p = 0.8787 for sperm motility. Center line represents the mean and error bars represent standard deviation. Each dot represents a measurement from a single animal. (**f**) Immunofluorescence of adult $P1^{+/+}$ or $P1^{V5/+}$ testes cross sections illustrates specificity of staining for the V5 tag. Scale bars: 20 µm. Shown are representative images and similar results were obtained from n = 3 independent experiments. (**g**) Immunoblots of subcellular fractions of elongating spermatids from synchronized testes lysates (days 23 and 24 post RA) for total P1 (V5-P1) and P1 K49ac. MNase, 0.5 M NaCl, 1 M NaCl, 2 M NaCl, and pellet represent nuclear fractions of increasing inaccessibility. Shown are representative immunoblots and similar results were obtained from n = 4 independent experiments. (**h**) Immunofluorescence of synchronized testes cross-sections days 23 and 24 post RA. Scale bars: 20 µm. Shown are representative images and similar results were obtained from n = 4 independent experiments.

https://doi.org/10.1038/s41594-023-01033-4

A

Genomic location	Number of mismatches	Sequence (including mismatches)	Genomic location
Chr6: 129535854	0	GCAGTGGCTCATACACCATAGGG	Intergenic
Chr12: 27066405	0	GCTACCACTCTTACACCATAGGG	Intergenic
Chr12: 5373801	0	GCCGCCTCGCAAACACCATAGGG	Intron: *Klhl29*
Chr10: 129362223	0	GCTGTCGATAATACACCATAGAG	Intergenic
Chr14: 102981772	0	ACCGCGGCTCCTACACCATCGGG	Exon: *Kctd12*
Chr6: 72119256	0	GCAGCCTCTCCTACACAATAAGG	Intron: *St3gal5*
Chr1: 167267189	0	GCCCCCTCCCATACACCACAGGG	Intron: *Uck2*
Chr2: 168467316	0	GCCACCACTCAGACACCAGATGG	Intergenic
Chr12: 4868024	0	GTCGCCCCTCATCCACAATAAGG	Intron: *Mfsd2b*

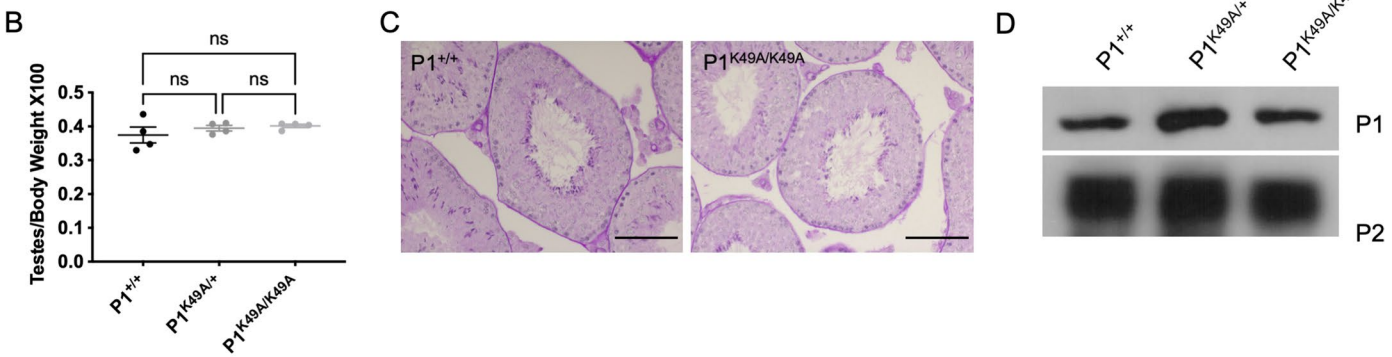

Extended Data Fig. 2 | P1 K49A substitution results in sperm motility defects and subfertility. (a) List of potential off-targets and corresponding sequencing results verify no off-target modifications generated by CRISPR/Cas9 editing. **(b)** Testes/body weight ratio of $P1^{+/+}$, $P1^{K49A/+}$, and $P1^{K49A/K49A}$ males (n = 4 per genotype) suggests no loss of germ cell populations due to P1 K49A substitution. Each dot represents a measurement from a single animal. Statistical test was performed using a one-way ANOVA and adjusted for multiple comparisons. Center line represents the mean and error bars represent standard deviation. **(c)** Periodic acid Schiff (PAS)-stained adult testes cross sections highlights normal testis morphology in $P1^{K49A/K49A}$ males. Scale bars: 50 µm. Shown are representative images and similar results were obtained from n = 2 males. **(d)** Acid urea immunoblot of acid-extracted testes from $P1^{+/+}$, $P1^{K49A/+}$, and $P1^{K49A/K49A}$ males shows comparable expression of P1 across all genotypes. Shown are representative immunoblots and similar results were obtained from n = 2 independent experiments.

https://doi.org/10.1038/s41594-023-01033-4

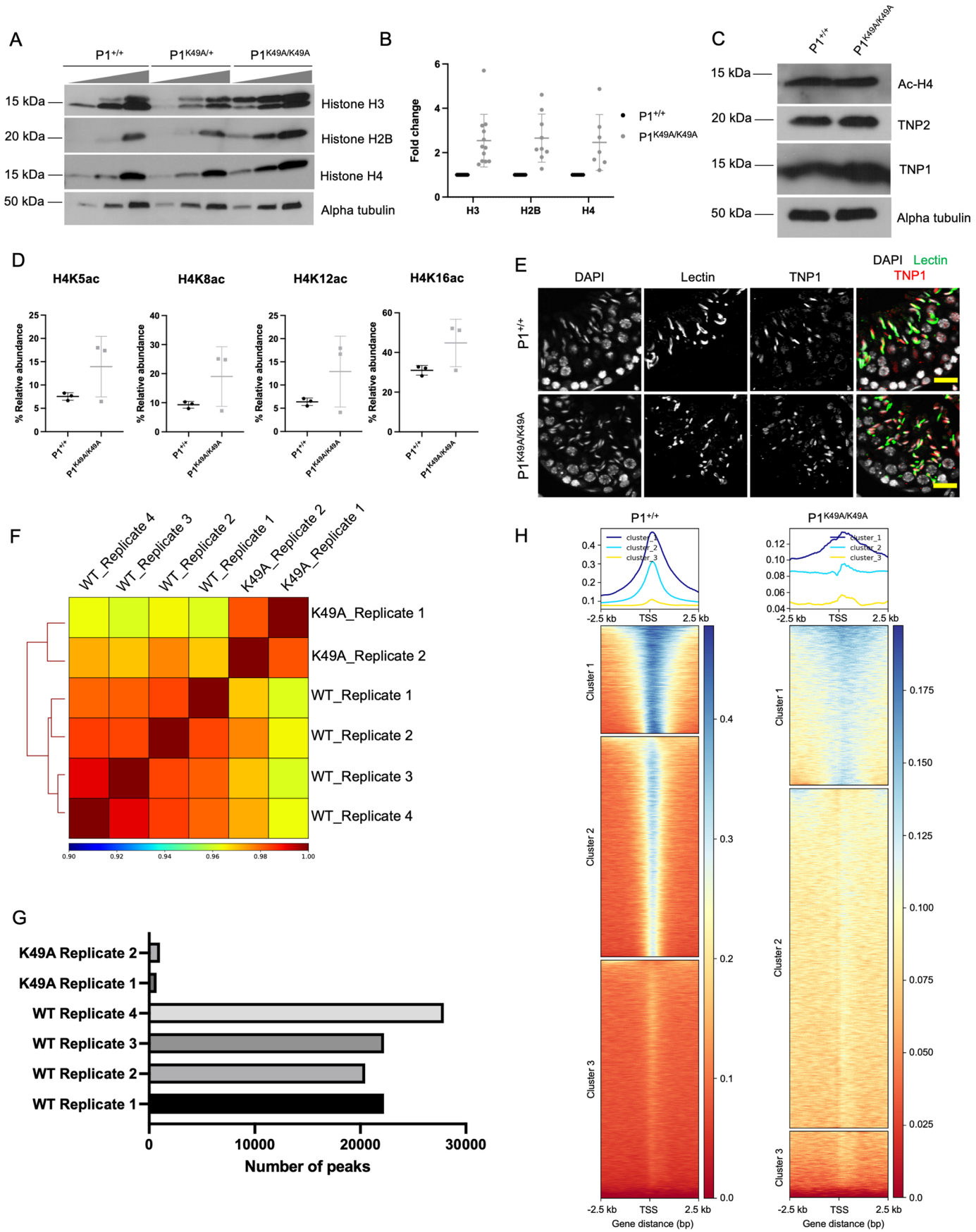

Extended Data Fig. 3 | See next page for caption.

https://doi.org/10.1038/s41594-023-01033-4

Extended Data Fig. 3 | P1 K49A substitution results in abnormal histone retention and altered histone PTMs in mature sperm. **(a)** Immunoblotting of sperm protein extracts reveals an abnormal retention of histones in $P1^{K49A/K49A}$ sperm. Blots were loaded by total input sperm number. Exact sperm numbers for the various antibodies provided in Methods section. **(b)** Quantification of immunoblots showing fold change of histone retention in $P1^{K49A/K49A}$ males. Data were collected from sperm from a total of n = 3 independent males per genotype. Across the 3 biological replicates, a total of n = 12 technical replicates were performed for H3, n = 9 technical replicates for H2B, and n = 7 technical replicates for H4. Each dot represents a single technical replicate measurement. Center line represents the mean and error bars represent standard deviation. **(c)** Immunoblots of protein lysates from $P1^{+/+}$ and $P1^{K49A/K49A}$ elongating spermatid-enriched testes lysate illustrates no difference in ac-H4, TNP2, or TNP1 levels. Shown are representative immunoblots and similar results were obtained from n = 2 independent experiments. **(d)** Quantification of abundance of histone H4 K5/K8/K12/K16 acetylation retained in $P1^{+/+}$ and $P1^{K49A/K49A}$ sperm. Each dot represents measurement from a single technical replicate (n = 3 technical replicates per genotype). Each biological sample (n = 1 per genotype) was prepared from a pool of sperm from n = 5 males per genotype. Center line represents the mean and error bars represent standard deviation. **(e)** Immunofluorescence staining of adult $P1^{+/+}$ or $P1^{K49A/K49A}$ testes cross sections stained for TNP1. Scale bars: 20 µm. Shown are representative images and similar results were obtained from n = 3 independent males. **(f)** Pearson correlation and hierarchical clustering shows high correlation between replicates and between WT and mutant datasets. **(g)** Number of peaks identified in each replicate dataset. **(h)** Genome-wide distribution of MNase-seq reads with respect to transcriptional start sites (TSS) of coding genes from mm10 reference genome. The region in the map is centered at the TSS and spans 2.5 kb on both sides of the TSS. Average profiles across gene regions ±2.5 kb for MNase-seq reads are shown on top.

https://doi.org/10.1038/s41594-023-01033-4

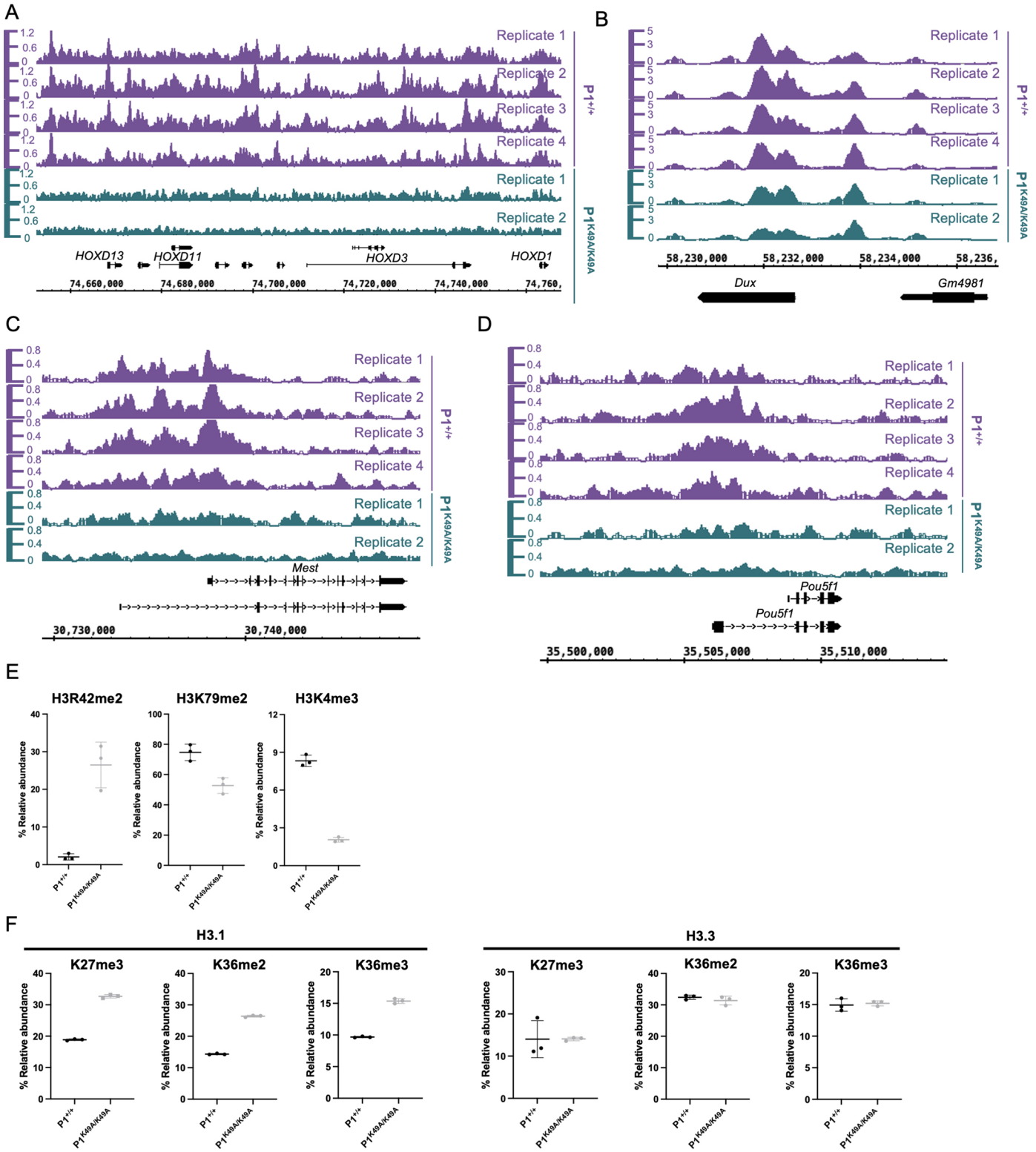

Extended Data Fig. 4 | P1 K49A sperm exhibit less fixed histone retention patterns and altered histone PTMs. (a–d) Genome browser tracks of nucleosomes enriched at developmental loci and imprinted genes. **(e, f)** Quantification of abundance of various histone H3 PTMs retained in $P1^{+/+}$ and $P1^{K49A/K49A}$ sperm. Each dot represents measurement from a single technical replicate (n = 3 technical replicates per genotype) and each biological sample (n = 1 per genotype) was prepared from a pool of sperm from n = 5 males per genotype. Center line represents the mean and error bars represent standard deviation.

https://doi.org/10.1038/s41594-023-01033-4

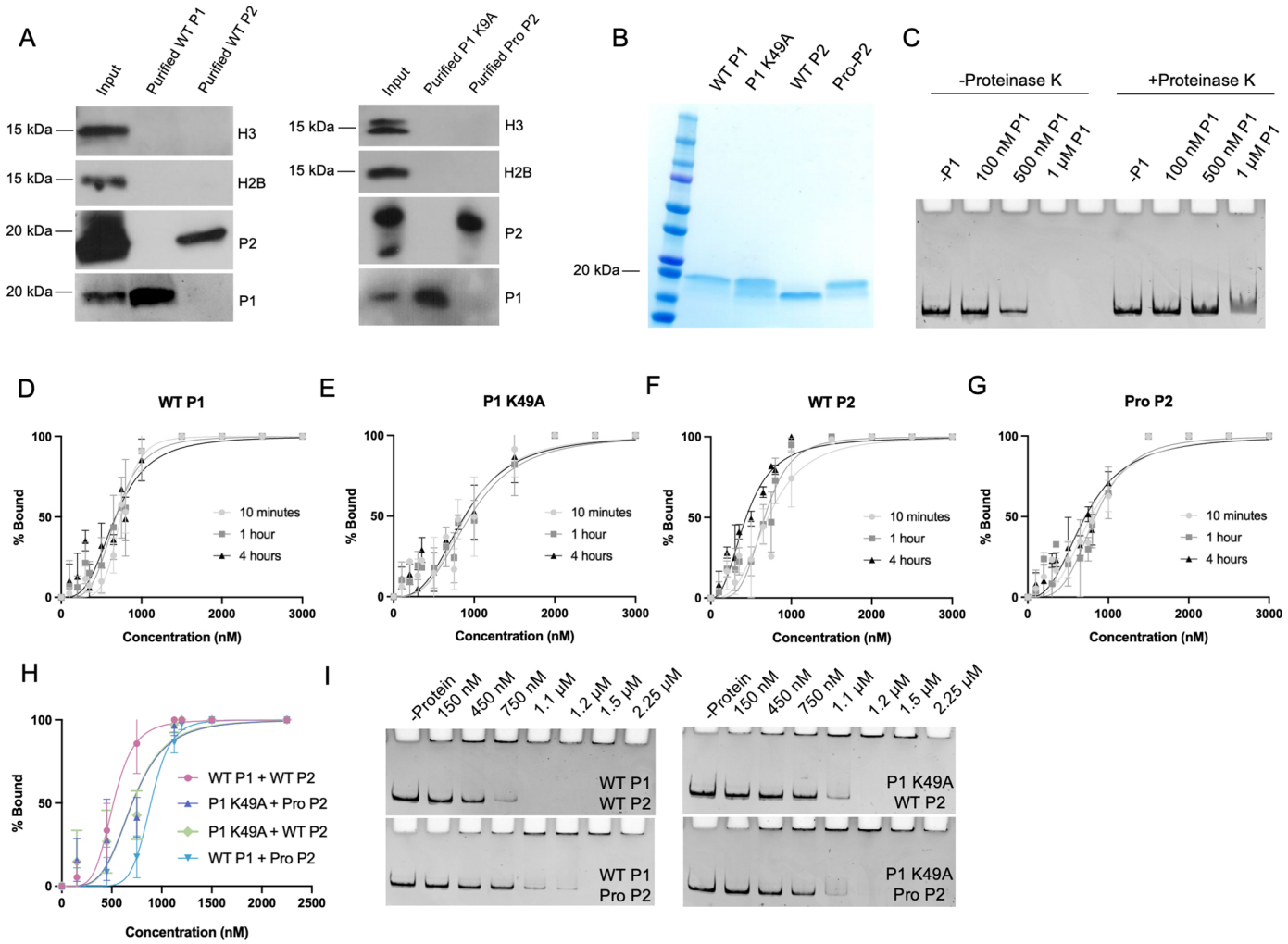

Extended Data Fig. 5 | Purified protamines are free of contaminating histones and their binding to DNA is unaffected by incubation time. (a) Immunoblot of input (prior to size exclusion chromatography) protein, purified P1 (WT or K49A), and purified P2 (WT or pro P2) illustrating efficient separation of P1 and P2 from each other and absence of histones in the final purified protein. Shown are representative immunoblots and similar results were obtained from n = 3 independent experiments. **(b)** Coomassie-stained SDS-PAGE gel of purified proteins illustrating high purity and equivalent concentrations. Shown is a representative gel and similar results were obtained from n = 4 independent experiments. **(c)** Proteinase K treatment of EMSA reactions after 1 hour of equilibration with DNA. **(d,e)** Quantification of binding affinities of WT P1 (d) and P1 K49A (e) after 10 minutes, 1 hour, or 4 hours of equilibration with DNA. Data are presented as an average of n = 4 technical replicates across n = 3 biologically independent samples for WT P1 10 minutes, n = 8 technical replicates across n = 3 biologically independent samples for WT P1 1 hour, n = 6 technical replicates across n = 3 biologically independent samples for WT P1 4 hours, n = 4 technical replicates across n = 3 biologically independent samples for P1 K49A 10 minutes, n = 9 technical replicates across n = 3 biologically independent samples for P1 K49A 1 hour, and n = 4 technical replicates across n = 3 biologically independent samples for P1 K49A 4 hours. Error bars represent standard deviation. **(f, g)** Quantification of binding affinities of WT P2 (f) and pro P2 (g) after 10 minutes, 1 hour, or 4 hours of equilibration with DNA. Data are presented as an average of n = 4 technical replicates across n = 3 biologically independent samples for WT P2 10 minutes, n = 9 technical replicates across n = 3 biologically independent samples for WT P2 1 hour, n = 4 technical replicates across n = 3 biologically independent samples for WT P2 4 hours, n = 3 technical replicates across n = 3 biologically independent samples for pro P2 10 minutes, n = 8 technical replicates across n = 3 biologically independent samples for pro P2 1 hour, and n = 4 technical replicates across n = 3 biologically independent samples for pro P2 4 hours. Error bars represent standard deviation. **(h)** Quantification of the binding affinities of P1 (either WT or K49A) and P2 (either WT or pro P2) mixed at a 1:2 ratio to a linear ~300 bp DNA fragment. Data are presented as an average of n = 4 technical replicates across n = 2 biologically independent samples for WT P1 + WT P2, n = 4 technical replicates across n = 2 biologically independent samples for WT P1 + pro P2, n = 3 technical replicates across n = 2 biologically independent samples for P1 K49A + WT P2, and n = 4 technical replicates across n = 2 biologically independent samples for P1 K49A + pro P2. Error bars represent standard deviation. **(i)** Representative EMSAs of titrations of increasing amounts of indicated P1 and P2 mixed at a 1:2 ratio. Data are presented as an average of n = 4 technical replicates for all protein combinations except P1 K49A + WT P2 (n = 3 technical replicates) across n = 2 biologically independent samples. Error bars represent standard deviation.

https://doi.org/10.1038/s41594-023-01033-4

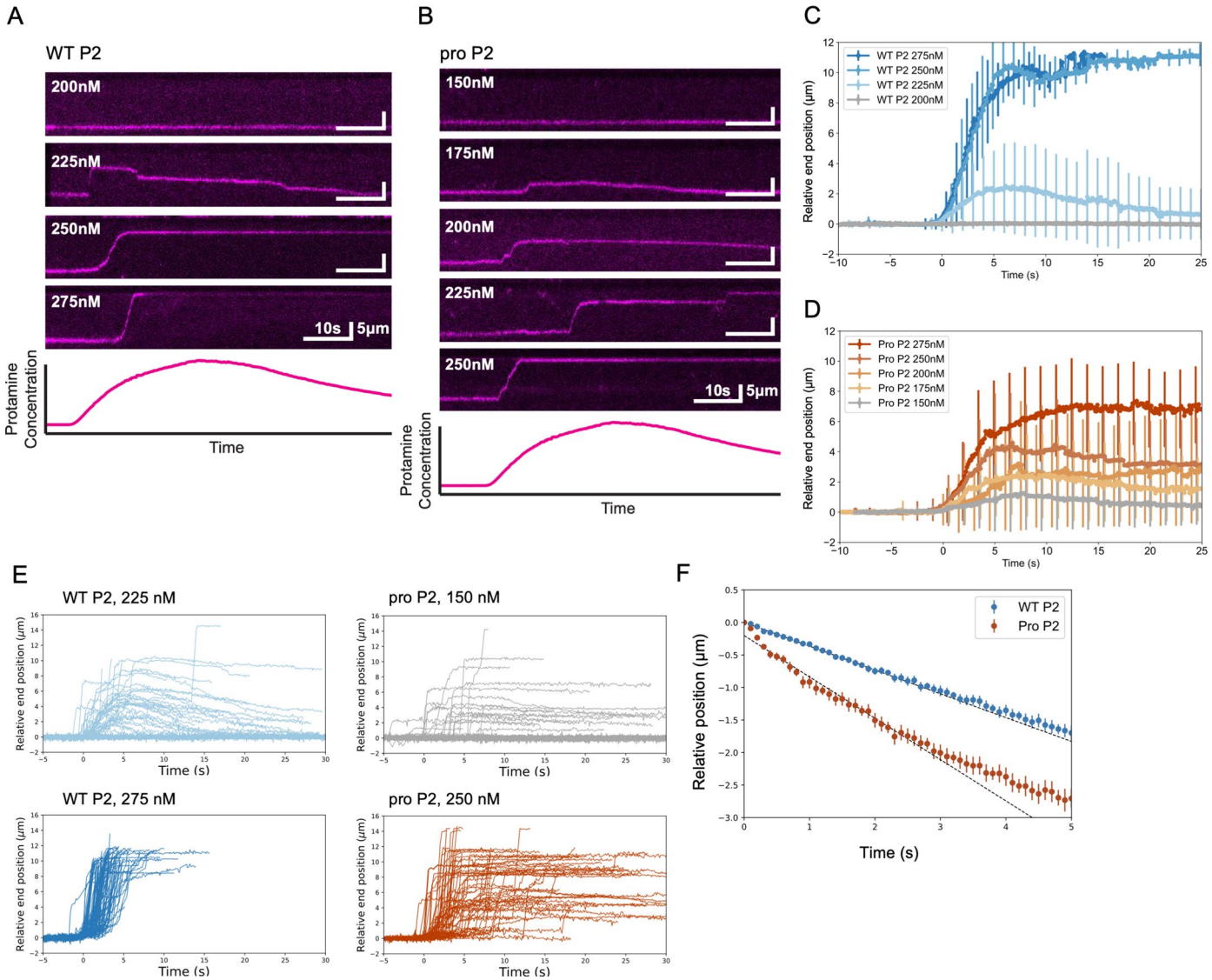

Extended Data Fig. 6 | P1 K49A substitution alters DNA compaction and decompaction kinetics *in vitro*. **(a)** Representative kymographs of WT P2 induced DNA compaction at increasing protein concentrations. **(b)** Representative kymographs of pro P2 induced DNA compaction at increasing protein concentrations. **(c)** Average DNA compaction by WT P2 at increasing concentrations. Error bars represent standard deviation (n = 71 traces for 200 nM, n = 63 for 225 nM, n = 95 for 250 nM, and n = 108 for 275 nM). **(d)** Average DNA compaction by pro P2 at increasing concentrations. Error bars represent standard deviation (n = 74 traces for 150 nM, n = 54 for 175 nM, n = 62 for 200 nM, n = 64 for 225 nM, and n = 65 for 250 nM). **(e)** Traces of individually tracked DNA molecules over time at low or high concentration of either WT P2 (left panels) or pro P2 (right panels) illustrating cooperative behavior. **(f)** Decompaction of DNA initially compacted by WT P2 and pro P2 over time illustrates differences in decompaction rates. Data were collected from n = 3 independent experiments (n = 3 flow cells per each independent experiment) for each protein. A total of n = 66 single DNA molecules were measured for WT P2 and n = 99 single DNA molecules were measured for pro P2. Error bars represent SEM.

https://doi.org/10.1038/s41594-023-01033-4

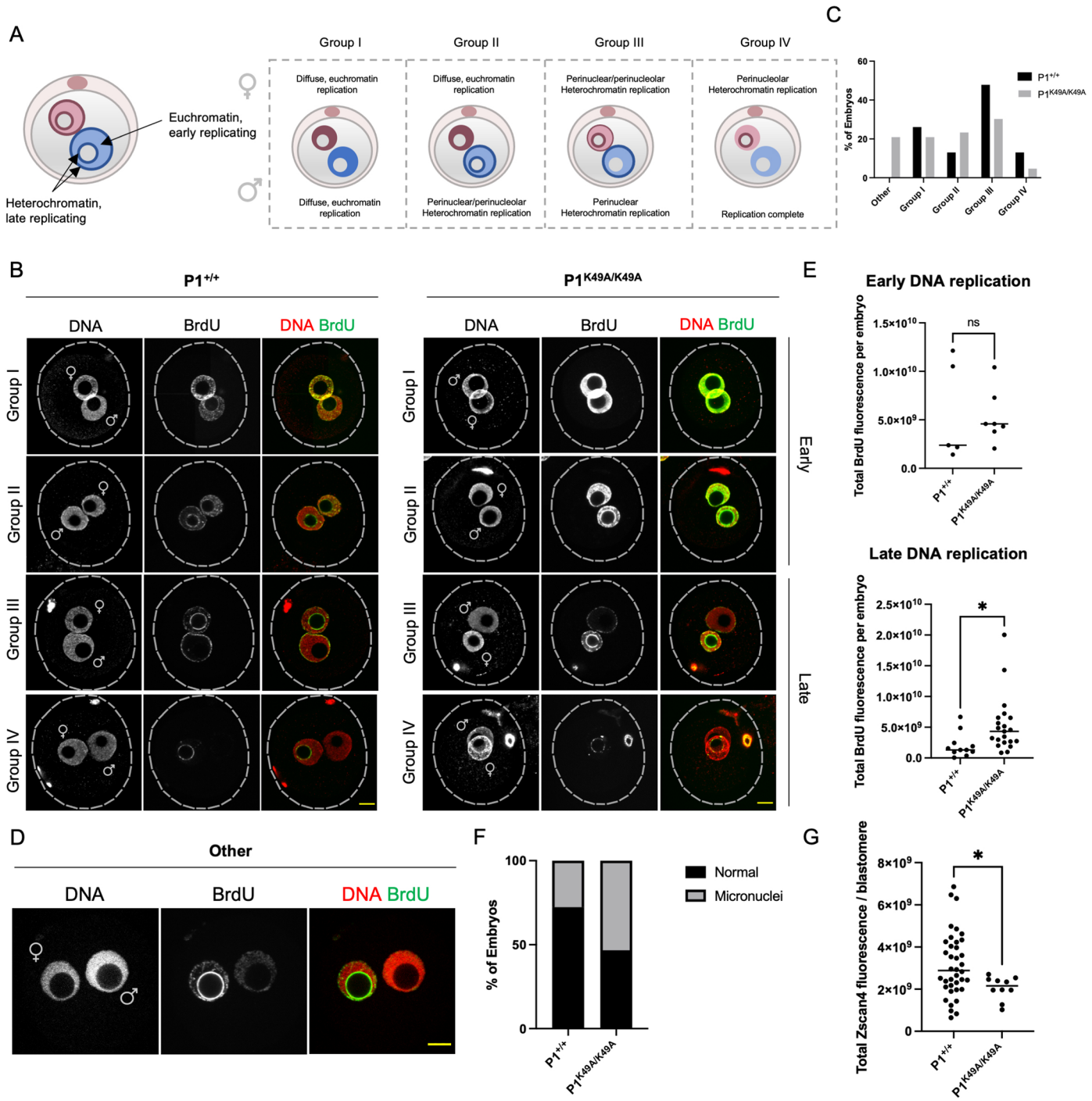

Extended Data Fig. 7 | P1 K49A substitution results in premature decompaction of paternal chromatin, altered DNA replication kinetics, and stalling at the zygote stage. (a) Cartoon representation of the four main stages of DNA replication in the mouse embryo as defined by Aoki and Schultz. **(b)** Immunofluorescence of zygotes collected 8.5 hpf and stained for BrdU. Representative images from each category are shown for both genotypes. Male and female pronuclei were identified based on proximity to the polar body (female being closer). Scale bars: 10 µm. Shown are representative images and similar results were obtained from n = 3 independent experiments. **(c)** Percent of WT and mutant embryos belonging to each category of DNA replication as defined in panel a. **(d)** Representative mutant embryo exhibiting altered DNA replication kinetics belonging to the 'other' category. Scale bar: 20 µm. Shown are representative images and similar results were obtained from n = 3 independent experiments. **(e)** Total fluorescence intensity measurements of BrdU per embryo indicates normal progression of DNA replication through early replication, but a stalling in late replication. Intensity measurements were taken from a total of n = 5 early replicating $P1^{+/+}$ embryos, n = 7 early replicating $P1^{K49A/K49A}$ embryos, n = 11 late replicating $P1^{+/+}$ embryos, and n = 21 late replicating $P1^{K49A/K49A}$ embryos. Statistical tests were performed using an unpaired, two-tailed t-test, p = 0.0325 for late replication. Center line represents the median. **(f)** Proportion of WT and mutant embryos collected at 30 hours post ICSI injection containing micro or multiple nuclei. **(g)** Total Zscan4 fluorescence intensity per blastomere for WT and mutant 2 cell embryos collected 26-30 hours post fertilization highlights a decrease in Zscan4 protein in mutant embryos. Intensity measurements were taken from a total of n = 38 $P1^{+/+}$ blastomeres and a total of n = 10 $P1^{K49A/K49A}$ blastomeres. Statistical test was performed using an unpaired, two-tailed t-test, p = 0.0339. Center line represents the median.

nature portfolio

Corresponding author(s): Saher Sue Hammoud

Last updated by author(s): May 11, 2023

Reporting Summary

Nature Portfolio wishes to improve the reproducibility of the work that we publish. This form provides structure for consistency and transparency in reporting. For further information on Nature Portfolio policies, see our Editorial Policies and the Editorial Policy Checklist.

Statistics

For all statistical analyses, confirm that the following items are present in the figure legend, table legend, main text, or Methods section.

n/a	Confirmed
☐	☒ The exact sample size (*n*) for each experimental group/condition, given as a discrete number and unit of measurement
☐	☒ A statement on whether measurements were taken from distinct samples or whether the same sample was measured repeatedly
☐	☒ The statistical test(s) used AND whether they are one- or two-sided *Only common tests should be described solely by name; describe more complex techniques in the Methods section.*
☒	☐ A description of all covariates tested
☐	☒ A description of any assumptions or corrections, such as tests of normality and adjustment for multiple comparisons
☐	☒ A full description of the statistical parameters including central tendency (e.g. means) or other basic estimates (e.g. regression coefficient) AND variation (e.g. standard deviation) or associated estimates of uncertainty (e.g. confidence intervals)
☐	☒ For null hypothesis testing, the test statistic (e.g. *F*, *t*, *r*) with confidence intervals, effect sizes, degrees of freedom and *P* value noted *Give P values as exact values whenever suitable.*
☒	☐ For Bayesian analysis, information on the choice of priors and Markov chain Monte Carlo settings
☒	☐ For hierarchical and complex designs, identification of the appropriate level for tests and full reporting of outcomes
☐	☒ Estimates of effect sizes (e.g. Cohen's *d*, Pearson's *r*), indicating how they were calculated

Our web collection on statistics for biologists contains articles on many of the points above.

Software and code

Policy information about availability of computer code

Data collection

All immunofluorescence images were collected using a Nikon A1R-HD25 confocal microscope.

For protamine PTM MS analysis, digests were analyzed by nano LC/MS/MS with a Waters NanoAcquity HPLC system interfaced to a ThermoFisher Q Exactive. The mass spectrometer was operated in data-dependent mode, with MS and MS/MS (15 most abundance ions) performed in the Orbitrap at 70,000 FWHM and 17,500 FWHM resolution, respectively.

For bottom-up MS analysis of quantitative histone retention, targeted LC-MS/MS was performed on a Thermo TSQ Altis (Thermo Scientific).

Single embryo RNA-seq samples were subjected to 150 bp paired-end sequencing on the NovaSeq6000 (Illumina platform).

Data analysis

Images were analyzed with ImageJ/Fiji version 1.52g and GraphPad Prism version 8 was used for statistical analysis.

For generation of P1 K49A mice, guide RNA target sequence was selected according to the on- and off-target scores provided by the web tool CRISPOR (v. 5.01).

The phylogenetic tree was constructed using maximum likelihood (PhyML) inferred from P1 protein sequences for species across the orders Rodentia, Primate, and Artiodactyla using the Whelan and Goldman matrix (WAG) substitution strategy. Sequences were downloaded from NCBI and aligned using standard parameters of MUSCLE.

For MS analysis, data were searched using a local copy of Byonic using the Swissprot Mouse database. Files were parsed into the Scaffold software for validation (v. 4.0.1).

For bottom-up MS analysis of quantitative histone retention, raw data were analyzed in Skyline (v 2.0).

For MNase-Seq, reads were trimmed using cta (v. 0.1.2; https://github.com/ParkerLab/cta). Reads were aligned to the mouse genome assembly mm10 using bwa mem (v. 0.7.15; -I 200,200,5000 -M). Duplicates were removed using Picard MarkDuplicates (v. 2.18.27; http://broadinstitute.github.io/picard) and samtools (v.1.7) was used to filter for properly paired and mapped reads pairs with mapping quality > = 30. Peaks were called using MACS2 callpeak (v. 2.1.1.20160309; options: --nomodel --broad --shift -100 --extsize 200 --keep-dup all). Peaks were filtered against ENCODE blacklists using bedtools intersect (option -v; v. 2.27.1). Metagene plots and heatmaps were made using deeptools (v 3.5.1). Venn digram was generated using R package VennDiagram(v 1.7.3). For analysis of AT vs. GC peak enrichment, peaks were fractionated into shared and disjoint sets (WT-only and K49A-only) using bedtools intersect. Peaks were annotated with their GC and AT content using bedtools nuc. These data were loaded into an R dataframe and summarized into density plots with ggplot2.

For single embryo RNA-seq samples, Bcl2fastq2 Conversion Software (Illumina) was used to generate demultiplexed Fastq files. Sequencing reads were trimmed using Cutadapt v2.3. FastQC v0.11.8 was used to ensure data quality and Fastq Screen v was used to screen for contamination. Reads were mapped to the reference genome GRCm38 using STAR v2.7.8a and assigned count estimates to genes with RSEM v1.3.3.

Analysis of DNA curtain data was performed with the following code generated in this study, available here: https://github.com/ReddingLab/Moritz_et_al_2021.

For manuscripts utilizing custom algorithms or software that are central to the research but not yet described in published literature, software must be made available to editors and reviewers. We strongly encourage code deposition in a community repository (e.g. GitHub). See the Nature Portfolio guidelines for submitting code & software for further information.

Data

Policy information about availability of data

All manuscripts must include a data availability statement. This statement should provide the following information, where applicable:

- Accession codes, unique identifiers, or web links for publicly available datasets
- A description of any restrictions on data availability
- For clinical datasets or third party data, please ensure that the statement adheres to our policy

Mass spectrometry proteomics data have been deposited to the ProteomeXchange Consortium via the PRIDE [1] partner repository with the dataset identifier PXD028917 and 10.6019/PXD028917 for protamine PTM analysis and via MassIVE with the dataset identifier MSV000091920 for histone MS. Analysis of MS data was achieved by searching against the Swissprot Mouse database for protamine PTMs. Given the large file size, raw DNA curtain videos are available upon request. All raw and processed genomic data files for single embryo sequencing and MNase-seq experiments are available under the GEO accession number GSE225271. For single embryo RNA-seq, our data were compared to previously published data across multiple embryonic stages (GSE45719). All relevant data is supplied in the Source Data.

Field-specific reporting

Please select the one below that is the best fit for your research. If you are not sure, read the appropriate sections before making your selection.

☒ Life sciences ☐ Behavioural & social sciences ☐ Ecological, evolutionary & environmental sciences

For a reference copy of the document with all sections, see nature.com/documents/nr-reporting-summary-flat.pdf

Life sciences study design

All studies must disclose on these points even when the disclosure is negative.

Sample size	Effect size was not predetermined. Sample size was determined according to published literature investigating similar topics (one example being a study by Luense et. al. - https://doi.org/10.1016/j.devcel.2019.10.024 ; another example is a study by Cho et. al. - DOI: 10.1038/ng0501-82, another example is a study by Schneider et. al. - DOI: 10.1038/srep36764, and the last example is a study by Takeda et. al - DOI: 10.1038/srep27409), to detect differences that are statistically significant. Statistical significance is indicated where applicable, along with statistical test used.
Data exclusions	No data were excluded, from analyses, aside from a select number of embryos for single-embryo RNA-seq that did not meet QC thresholds
Replication	All experiments, when possible, were reproduced at least three times with independent biological/technical samples unless otherwise specified in the figure. One exception is the ICSI experiments. The data from ICSI are from two independent replicas from at least 5 pooled females and three pooled sperm samples. The data are highly reproducible across genotypes.
Randomization	Randomization of ICSI experiments was achieved by alternating injections between WT and K49A sperm. Experiments involving phenotyping analysis of male mice and sperm morphology assessment were randomized. Additionally, experiments involving quantification of immunofluorescent signal were randomized.
Blinding	Wherever experiments involved analysis of samples from different genotypes (i.e. WT vs. K49A), investigators were blinded to the genotype during collection.

Reporting for specific materials, systems and methods

We require information from authors about some types of materials, experimental systems and methods used in many studies. Here, indicate whether each material, system or method listed is relevant to your study. If you are not sure if a list item applies to your research, read the appropriate section before selecting a response.

Materials & experimental systems

n/a	Involved in the study
☐	☒ Antibodies
☒	☐ Eukaryotic cell lines
☒	☐ Palaeontology and archaeology
☐	☒ Animals and other organisms
☒	☐ Human research participants
☒	☐ Clinical data
☒	☐ Dual use research of concern

Methods

n/a	Involved in the study
☒	☐ ChIP-seq
☒	☐ Flow cytometry
☒	☐ MRI-based neuroimaging

Antibodies

Antibodies used

1. Rabbit anti-P1 K49ac (1:500 for IF and immunoblotting, generated in this study)
2. Mouse anti-Protamine 1 (1:500 for immunoblotting, Briarpatch Biosciences, Cat# Hup1N, RRID: AB_2651186)
3. Mouse anti-Protamine 2 (1:1000 for immunoblotting, Briarpatch Biosciences, Cat# Hup2B, RRID: AB_2687949)
4. Mouse anti-Histone H2B (1:1000, Abcam, Cat #ab52484, RRID: AB_1139809)
5. Rabbit anti-Histone H3 (1:1000, Abcam, Cat#, ab1791, RRID: AB_302613
6. Rabbit anti-Histone H4 (1:500, Protein Tech, Cat# 16047-1-AP, RRID: AB_2118625)
7. Rabbit anti-Tetra-Acetyl H4 (1:1000 for IF and immunoblotting, EMD Millipore, Cat# 06-866, RRID: AB_310270)
8. Mouse anti-Alpha tubulin (1:1000, Protein Tech, Cat# 66031-1-Ig, RRID: 11042766)
9. Rabbit anti-Tnp1 (1:100 for IF, 1:500 for immunoblotting, Protein tech, Cat# 17178-1-AP, RRID: AB_2206757)
10. Mouse anti-Tnp2 (1:1000 for IF and immunoblotting, Santa Cruz, Cat#sc- 393843, RRID: N/A)
11. Mouse anti-V5 (1:1000 for IF and immunoblotting, BioRad, Cat# MCA1360, RRID: AB_322378)
12. PNA-Lectin (1:1000, GeneTex, Cat# GTX01508, RRID: N/A)
13. Rat anti-BrdU (1:500, Abcam, Cat#ab6326, RRID: AB_305426)
14. Rabbit anti-Zscan4 (1:500, Abcam, Sigma, Cat#AB4340, RRID: AB_2827621)
15. Mouse anti-Phospho-H2A.X S139 (1:500, Millipore Sigma, Cat#05-636, RRID: AB_309864)

Validation

Validation of custom antibodies generated for this study are provided in Extended Data Fig. 1.

Commercially available antibodies have provided validation statements on their respective websites, information provided below for each antibody.

2. Mouse anti-Protamine 1 from Briarpatch Biosciences, Cat# Hup1N: https://briarpatchbio.com/wp-content/uploads/2014/06/ProtamineAntibodyInsert.pdf
3. Mouse anti-Protamine 2 from Briarpatch Biosciences, Cat# Hup2B: https://briarpatchbio.com/wp-content/uploads/2014/06/ProtamineAntibodyInsert.pdf
4. Mouse anti-Histone H2B from Abcam, Cat #ab52484: https://www.abcam.com/products/primary-antibodies/histone-h2b-antibody-mabcam-52484-chip-grade-ab52484.html
5. Rabbit anti-Histone H3 from Abcam, Cat#, ab1791: https://www.abcam.com/products/primary-antibodies/histone-h3-antibody-nuclear-marker-and-chip-grade-ab1791.html
6. Rabbit anti-Histone H4 from Protein Tech, Cat# 16047-1-AP: https://www.ptglab.com/products/HIST1H4E-Antibody-16047-1-AP.htm
7. Rabbit anti-Tetra-Acetyl H4 from EMD Millipore, Cat# 06-866: https://www.emdmillipore.com/US/en/product/Anti-acetyl-Histone-H4-Antibody,MM_NF-06-866
8. Mouse anti-Alpha tubulin from Protein Tech, Cat# 66031-1-Ig: https://www.ptglab.com/products/tubulin-Alpha-Antibody-66031-1-Ig.htm
9. Rabbit anti-Tnp1 from Protein tech, Cat# 17178-1-AP: https://www.ptglab.com/products/TNP1-Antibody-17178-1-AP.htm
10. Mouse anti-Tnp2 from Santa Cruz, Cat#sc- 393843: https://www.scbt.com/p/tnp2-antibody-b-2
11. Mouse anti-V5 from BioRad, Cat# MCA1360: https://www.bio-rad-antibodies.com/monoclonal/viral-v5-tag-antibody-sv5-pk1-mca1360.html?f=purified&JSESSIONID_STERLING=E87EFAA637DE8E6282AC7600D1517CD2.ecommerce1&evCntryLang=US-en&cntry=US&thirdPartyCookieEnabled=true
12. PNA-Lectin from Cat# GTX01508, RRID: https://www.genetex.com/Product/Detail/Peanut-Lectin-FITC/GTX01508
13. Rat anti-BrdU (1:500, Abcam, Cat#ab6326, RRID: AB_305426): https://www.abcam.com/products/primary-antibodies/brdu-antibody-bu175-icr1-proliferation-marker-ab6326.html
14. Rabbit anti-Zscan4 (1:500, Sigma, Cat#AB4340, RRID: AB_2827621): https://www.emdmillipore.com/US/en/product/Anti-Zscan4-Antibody,MM_NF-AB4340?CatalogCategoryID=&ReferrerURL=https%3A%2F%2Fwww.google.com%2F
15. Mouse anti-Phospho-H2A.X S139 (1:500, Millipore Sigma, Cat#05-636, RRID: AB_309864): https://www.emdmillipore.com/US/en/product/Anti-phospho-Histone-H2A.X-Ser139-Antibody-clone-JBW301,MM_NF-05-636

Animals and other organisms

Policy information about studies involving animals; ARRIVE guidelines recommended for reporting animal research

Laboratory animals

Mice were housed in the University of Michigan animal facility in an environment controlled for light (12 hours on/off), temperature (21 to 23oC), and humidity (30-70%) with ad libitum access to water and food (Lab Diet #5008 for breeding mice, #5LOD for non-breeding animals).

Various mouse (Mus musculus) strains (including mutants generated for this study) listed below were used in this study. Details can be found in the manuscript and methods.

C57BL/6 (The Jackson Laboratory #000664)
P1K49A/K49A (generated in this study)
P1V5/+ (generated in this study)
P1K49R/K49R (generated in this study)
P1Δ46-51/Δ46-51 (generated in this study)
B6D2F1/J (The Jackson Laboratory #100006)

C57BL6/J, P1K49A/K49A, P1 V5/+, P1K49R/K49R, and P1Δ46-51/Δ46-51: only males of 8-16 weeks were used for experiments and females 8-16 weeks of age from these lines were used solely for breeding.

B6D2F1/J: 8 week old females were used for oocyte collection for ICSI.

Wild animals

Our study did not involve wild animals.

Field-collected samples

Our study did not involve field-collected samples.

Ethics oversight

For generation of P1 K49A, P1 K49R, and P1Δ46-51 mice, all animal procedures were carried out in accordance with the Institutional Animal Care and Use Committee and approval of Cincinnati Children's Hospital Medical Center.

For all other experiments, all experiments using animals were carried out with prior approval of the University of Michigan Institutional Committee on Use and Care of Animals (Protocols: PRO00006047, PRO00008135, PRO00010000) and in accordance with the guidelines established by the National Research Council Guide for the Care and Use of Laboratory Animals.

Note that full information on the approval of the study protocol must also be provided in the manuscript.